

PRECISION SPECTROSCOPY FOR 1.9 MILLION GALAXIES FROM SDSS-IV: IMPROVED SPECTRAL MEASUREMENTS AND CATALOGS FOR EBOSS

OWEN S. MATTHEWS ACUÑA*¹, CHRISTY A. TREMONTI¹, KYLE B. WESTFALL², SHEA DEFOUR-REMY^{1,3},
ALEKSANDAR M. DIAMOND-STANIC⁴, ZACH J. LEWIS¹, BRITT LUNDGREN⁵, DRAKE MILLER III^{1,6}, LIZHOU SHA¹

¹Department of Astronomy, University of Wisconsin—Madison, Madison, WI 53706, USA

²University of California Observatories, University of California, Santa Cruz, 1156 High Street, Santa Cruz, CA 95064, USA

³Steward Observatory, University of Arizona, Tucson, AZ 85719, USA

⁴Department of Physics and Astronomy, Bates College, Lewiston, ME 04240, USA

⁵Department of Physics and Astronomy, University of North Carolina Asheville, Asheville, NC 28804, USA

⁶Department of Astrophysical and Planetary Sciences, University of Colorado Boulder, Boulder, CO 80309, USA

Version December 23, 2025

ABSTRACT

The Sloan Digital Sky Survey IV DR17 Extended Baryon Oscillation Spectroscopic Survey (eBOSS) consists of 2,233,939 high-quality optical galaxy spectra obtained through 2" fibers, providing a rich spectroscopic resource for studying galaxy evolution across a broad redshift range. eBOSS was designed primarily for large-scale structure and BAO measurements and, as such, focused on galaxy redshifts, leaving much of the information contained in the spectra unexplored. In addition to the trove of spectra, the large number of repeat observations (197,521 duplicate spectra) enables evaluation of the survey's spectrophotometric quality. To unlock this potential, we introduce the eBOSS Data Analysis Pipeline (eBOSS-DAP), adapted from the MaNGA-DAP, which delivers uniform measurements of emission-line fluxes and equivalent widths, stellar and gas kinematics, continuum spectral indices, and stellar population fits. Using the eBOSS-DAP, we successfully analyze 1,899,553 high-quality galaxy spectra below a redshift of $z < 1.12$ to produce an extensive spectroscopic catalog for the eBOSS galaxy sample. We characterize the calibration performance, quantify the reliability of the derived measurements, and release a suite of data products that fully exploit the power of the eBOSS dataset. These catalogs open the door to a new generation of studies in galaxy evolution and cosmology.

Keywords: galaxies: Emission Line Catalog, Absorption Index Catalog

1. INTRODUCTION

The era of publicly available big data, such as the first Sloan Digital Sky Survey data release (SDSS-I; D. G. York et al. 2000), has demonstrated that innovative applications of surveys beyond their intended scope can lead to significant advancements in astronomy. Initially designed to study large-scale structures, SDSS-I was quickly used to further the field of galaxy evolution studies following the release of the MPA-JHU catalog of galaxy emission lines, star formation rates, and stellar masses (J. Brinchmann et al. 2004).

The MPA-JHU catalog enabled one of the first analyses of the star formation main sequence at $z \sim 0.1$ (J. Brinchmann et al. 2004). These data were also used to study the stellar mass–metallicity relation (C. A. Tremonti et al. 2004; L. J. Kewley & S. L. Ellison 2008; B. H. Andrews & P. Martini 2013), the fundamental metallicity relation (F. Mannucci et al. 2010; S. Salim et al. 2014), the properties of Type II Active Galactic Nuclei (AGN) (G. Kauffmann et al. 2004; T. M. Heckman et al. 2004; L. J. Kewley et al. 2006), and the impact

of galactic environment on galaxy evolution (G. Kauffmann et al. 2004; S. M. Weinmann et al. 2006; M. R. Blanton & J. Moustakas 2009; Y.-j. Peng et al. 2010).

The SDSS-IV Extended Baryon Oscillation Spectroscopic Survey (eBOSS; K. S. Dawson et al. 2016a), a component of Sloan Digital Sky Survey IV (SDSS IV; M. R. Blanton et al. 2017), is the successor of SDSS I-III. Intending to map the Universe's structure by studying galaxies, quasi-stellar objects (QSOs), and the Lyman-alpha forest, eBOSS sports a much broader and higher redshift range than SDSS-I. eBOSS produced about 4 million spectra, providing a rich resource for studying galaxy and QSO properties at various redshifts. However, unlike the SDSS-I catalog, eBOSS has only been used for a few galaxy evolution studies to date (c.f., G. B. Zhu et al. 2015; T.-W. Lan & H. Mo 2018; A. Anand et al. 2021). One reason is the lack of a high-quality and well-documented emission line catalog. The current eBOSS emission line catalog (`spZline` files) provides only 18 emission lines and has relatively minimal documentation of the critical facets of the stellar continuum and emission line fitting routines (A. S. Bolton et al. 2012). Additionally, this catalog used empirical rather than theoretical stellar population templates (See

§3.2.2) and Principal Component Analysis to fit the stellar continuum rather than stellar population modeling.

There are three primary goals in this work: 1) to provide an overview of the properties of the eBOSS galaxy sample; 2) to characterize the spectroscopic calibration of the survey; and 3) to measure and produce a catalog of emission lines, spectral indices, and stellar kinematics. eBOSS is a combination of at least seven different individual surveys, thus giving the eBOSS galaxy sample unique and complex characteristics beyond those of other comparable surveys (K. S. Dawson et al. 2013). To analyze the survey calibration, we make use of a unique facet of the eBOSS sample: duplicate spectra. eBOSS has a remarkable quantity of repeat observations of single objects, allowing us to assess the precision of the spectrophotometric calibration. Our final goal, to provide a catalog of emission lines, spectral indices, and stellar kinematics, is accomplished through the creation of the eBOSS - Data Analysis Pipeline (eBOSS-DAP). The eBOSS-DAP was built from the well-vetted algorithms developed for the Mapping Nearby Galaxies at Apache Point Observatory - Data Analysis Pipeline (MaNGA-DAP; K. B. Westfall et al. 2019; F. Belfiore et al. 2019).

An outline of the paper is as follows: In Section 2, we discuss the properties of the eBOSS galaxy sample and we quantify the survey’s spectrophotometric quality. Then, in Section 3, we describe how we have adapted the MaNGA-DAP to work with eBOSS data and we outline eBOSS-DAP workflow. Next, in Section 4, we discuss the eBOSS-DAP’s results and provide some figures that demonstrate the scientific potential of the data. Finally, we provide a brief summary in Section 5.

The data products detailed in the paper are publicly available through the NOIRLab Astro Data Lab (M. J. Fitzpatrick et al. 2014; R. Nikutta et al. 2020). The source code, spectral template models, and customized emission line lists are available on GitHub. Details of the data/code access are described in Data Availability.

2. DATA

2.1. SDSS-IV Data

The galaxy spectra analyzed in this work are drawn from the Sloan Digital Sky Survey (D. G. York et al. 2000) Data Release 17 (SDSS DR17; Abdurro’uf et al. 2022a). SDSS-I obtained imaging of $\sim 1/4$ of the sky in the *ugriz* filters (M. Fukugita et al. 1996) with a drift scan imaging camera (J. E. Gunn et al. 1998) mounted in the SDSS 2.5-m telescope (J. E. Gunn et al. 2006) at Apache Point Observatory. The *ugriz* photometry (R. Lupton et al. 2001) was used to target a variety of stars, galaxies, and quasars for follow-up spectroscopy (C. Stoughton et al. 2002).

In this work, we focus on the roughly 2 million spectra obtained as part of the SDSS-III Baryon Oscillations Spectroscopic Survey (BOSS; D. J. Eisenstein et al. 2011) and the SDSS-IV Extended Baryon Oscillation Spectroscopic Survey (eBOSS; K. S. Dawson et al. 2016b). The

goal of BOSS and eBOSS¹ was to map the 3D structure of the universe to measure baryon acoustic oscillations at different redshifts (c.f. D. J. Eisenstein et al. 2005).

This was accomplished by targeting three different types of objects for spectroscopy based on their photometric colors: Luminous Red Galaxies (LRGs) in several different redshift slices (D. J. Eisenstein et al. 2001; B. Reid et al. 2016; A. Prakash et al. 2016); Emission Line Galaxies (ELGs) at $z \sim 0.6 - 1.1$ (A. Raichoor et al. 2017, 2021), and Quasars at $0.9 < z < 2.2$ (A. D. Myers et al. 2015). SDSS-IV also conducted two smaller programs, (SPIDERS; N. Clerc et al. 2016; T. Dwelly et al. 2017) and (TDSS; E. Morganson et al. 2015) which target X-ray sources and variable objects respectively.

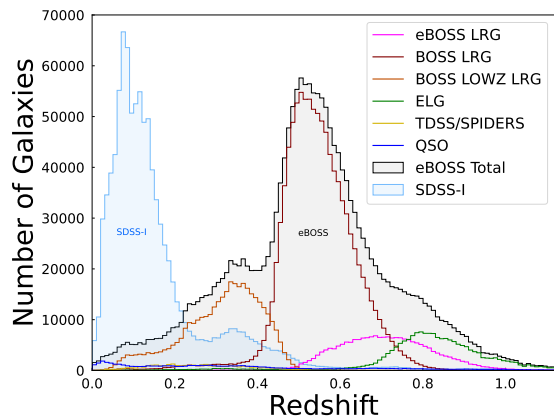


Figure 1. Redshift distribution of the SDSS-I (light blue) and eBOSS (gray) galaxy samples. The eBOSS galaxies are further divided based on how they were targeted for spectroscopy. LRGs are Luminous Red Galaxies; these galaxies are further broken down by the survey from which they originate. ELGs are Emission Line Galaxies and take up a large portion of our sample at the highest redshifts. TDSS/SPIDERS are targeted based on variable photometry and X-ray data. Finally, the histogram labeled QSO represents objects that were initially targeted as quasars but, upon further analysis, were revealed to be compact blue galaxies. In total, the eBOSS galaxy sample peaks at $z = 0.55$ and contains 1,901,834 spectra. For comparison, the SDSS-I galaxy sample contains 987,729 spectra with two peaks at $z = 0.1$ and $z = 0.35$.

Targets were observed through 2” diameter optical fibers positioned at the SDSS telescope’s focal plane using custom-drilled aluminum ‘plates’ that span 3 degrees on the sky. The plates enable one thousand targets (900 objects, 80 sky, 20 standard stars) to be observed simultaneously. The hole positions for fibers placed on galaxy and standard star targets were centered to account for predicted atmospheric differential refraction (A. V. Filippenko 1982a). For the majority of the survey, fibers were centered to maximize throughput for 5400 Å light. However, fibers on plates targeting ELGs were centered on the predicted position for 7500 Å light to maximize throughput for redshifted [OII] $\lambda 3727$. In addition, some quasar targets were centered to maximize throughput at 4000 Å for Lyman-alpha forest studies.

¹ Hereafter, we will reference the sum of both of these surveys as eBOSS.

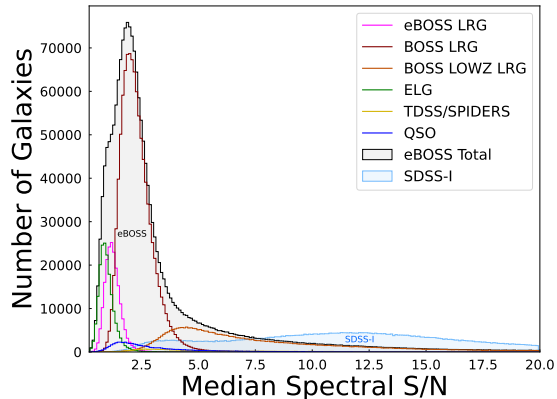


Figure 2. Median signal-to-noise (S/N) per pixel distribution of the SDSS-I (light blue) and eBOSS (gray) galaxy spectra. The eBOSS galaxies are further divided based on how they were targeted for spectroscopy. In total, the eBOSS galaxy sample peaks at $S/N = 1.88$. For comparison, the SDSS-I galaxy sample has two peaks at $S/N = 3.9$ and $S/N = 12.1$.

The light from the fibers was sent to the upgraded SDSS-BOSS spectrographs (S. A. Smee et al. 2013; K. S. Dawson et al. 2013), which have wavelength coverage from $3610 - 10140 \text{ \AA}$ at a spectral resolution of $R = 1560 - 2650$. Spectra were reduced by the `idlSpec2D` pipeline version `v5_13_2`² (K. S. Dawson et al. 2016b). The `spectro1d` pipeline classified each eBOSS spectrum as a star, galaxy, or quasar and measured its redshift (A. S. Bolton et al. 2012).

2.2. Sample Selection

We selected our sample using the SDSS DR17 summary file `spAll-v5_13_2`. We chose spectra that were classified as galaxies (`CLASS = GALAXY`), resulting in 2,233,939 eBOSS galaxy spectra. The `GALAXY` class includes Type II AGN, but not Type-I (broadline) AGN (A. S. Bolton et al. 2012). We then selected only the galaxy spectra which met the SDSS survey quality standards (`PLATEQUALITY = GOOD`) and applied a redshift cut of $0.0005 < z < 1.12$ and required that no redshift warning flags were set (`ZWARNING=0`). The lower redshift limit ($\sim 150 \text{ km s}^{-1}$) eliminates some Milky Way stars that are mistakenly classified as galaxies. Our upper redshift limit was adopted because our fitting code requires either $H\alpha$ or $H\beta$ to fit the other emission lines (see §3.2.3) and $H\beta$ redshifts out of the spectra at $z \gtrsim 1.12$. With these quality and redshift cuts, we trim the 2,233,939 eBOSS galaxy spectra to a sample of 1,901,834. Of these spectra, 197,521 are duplicates (e.g., only 1,704,313 unique galaxies were observed) with the max number of duplicates being 64 for one object.

In Figure 1, we show the redshift distribution of our galaxy spectra with the sample divided and color-coded by target class. The listed target classes encompass several broad categories used to photometrically select the galaxies for follow-up spectroscopy. Details of the target selection for each object are preserved in the SDSS

`spAll` file and described in K. S. Dawson et al. (2016b) and references therein. The objects labeled ‘QSO’ were originally targeted as quasars but were spectroscopically classified as galaxies.

In Figure 2, we show the median signal-to-noise ratio (S/N) distribution of the eBOSS galaxy spectra in our sample divided and color-coded by target class. Both figures also show the distribution for the widely used SDSS-I sample. By comparing these two, we see that eBOSS is ~ 2 times larger with a much higher and wider redshift range while also being, on average, lower S/N than SDSS-I.

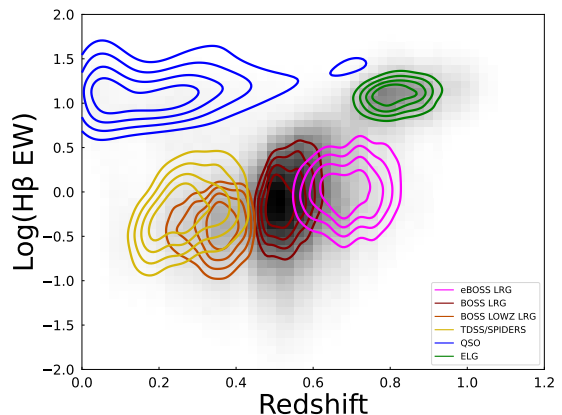


Figure 3. $H\beta$ emission line Equivalent Width vs. redshift for all six target categories and a 2D histogram of the full sample. The target contours begin at 50% of the data.

Additionally, we include an $H\beta$ emission line Equivalent Width (EW) vs. redshift diagram demonstrating the average redshifts and EWs, See §3.2.3 and §3.3, of each target classification (Figure 3). As shown in this figure, ELGS and QSOs have much higher EWs than the LRG portion of the sample, as expected based on their color-selection. Additionally, there is a small upward trend with redshift in the LRG sample where the higher z galaxies show marginally higher $H\beta$ EWs.

2.3. Aperture Bias

eBOSS observed galaxies through $2''$ diameter fibers and calibrated the spectra such that their fluxes would be correct for targets that were point sources. However, the majority of eBOSS galaxies are spatially extended, leading to some aperture bias and loss of light.

To quantify this effect, we computed the fraction of the total r -band galaxy light captured by the fiber by comparing synthetic photometry computed from the spectra (found in the `spAll` field `spectroflux`) to the observed photometry (`modelflux`). We explore trends between the fraction of light in the fiber, redshift, and galaxy target category in Figure 4. The fraction of light in the fiber ranges from $\sim 0.2 - 1.1$ with a median of 0.52. This is larger than the typical fraction of light in the fiber for SDSS-I galaxies (~ 0.3) since SDSS-I primarily targeted galaxies at lower redshifts ($z \lesssim 0.25$) (see Fig. 1.)

² https://svn.sdss.org/public/repo/eboss/idlSpec2d/tags/v5_13_2/

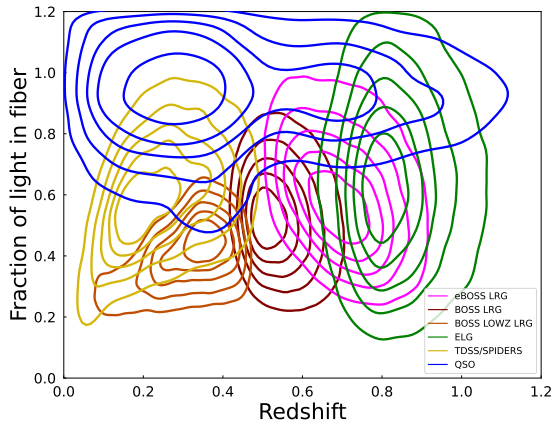


Figure 4. A two-dimensional kernel density estimate plot of the fraction of galaxy light encompassed by the SDSS fiber for the different target categories as a function of redshift. The fraction of light in the fiber is computed from the ratio of the SDSS r -band flux measured from the spectrum over that measured from photometry. This shows that different targeting categories are more likely to be fully captured by the fiber than others. The outer contours enclose 90% of the sample.

Galaxies that were targeted as QSOs (blue contours in Fig. 4) have large fractions of light in the fiber since many of the quasar target selection algorithms required them to be point sources. Notably, for most other target classes, the fraction of light in the fiber increases as a function of redshift due to the smaller apparent diameter of the galaxies. Roughly 5.3% of objects have a light fraction greater than 1, implying that the spectrum is brighter than expected from the imaging data. This comes about for three reasons: i) flux calibration errors in the spectra (see §2.4); ii) errors in the photometry, which is near the magnitude limit of the survey; and iii) errors in photometric deblending which cause large galaxies to be shredded into smaller pieces, causing the fluxes from the imaging data to be underestimated (i.e., an H II region in a nearby galaxy might be categorized as a compact galaxy; see Fig.8).

In summary, for a typical eBOSS galaxy, the spectrum captures 40 - 75% of the total galaxy light. This implies that the bias due to the finite fiber aperture is not extreme; the spectra are closer to global galaxy spectra than to nuclear spectra. However, it will be essential to correct for the missing light when computing absolute quantities such as $H\alpha$ -based star formation rates.

2.4. Spectrophotometric Quality

A major source of spectrophotometric calibration error for eBOSS — and most ground-based spectroscopic surveys — is atmospheric dispersion. Atmospheric dispersion occurs when light from celestial objects passes through the Earth’s atmosphere at an angle, causing the light to refract and spread out into its component colors. The resulting image is dispersed in a direction perpendicular to the horizon by an amount that depends on the elevation of the object. At an airmass of 1.5 (elevation of 42°), light at 4000 \AA and $1 \mu\text{m}$ are separated by about $1.7''$ (A. V. Filippenko 1982b). This can affect the accu-

racy of spectroscopic measurements made through small apertures that can miss a fraction of the highly dispersed blue or red light.

The eBOSS data are spectrophotometrically calibrated by the SDSS `id1spec2D` pipeline as described in K. Abazajian et al. (2004) and K. S. Dawson et al. (2016b). In brief, on any given plate, 20 color-selected ‘standard stars’ are observed. These A-to-G-type stars are not classical standards like those of J. B. Oke (1990) because their calibrated spectrum is unknown. Flux calibration is achieved by matching each star to a grid of stellar atmosphere models that have been rescaled to match the observed r -band PSF magnitude of the standard star. The use of multiple standards per plate (which are averaged with rejection) mitigates the effect of the occasional problematic star. The standard and object spectra experience approximately the same atmospheric dispersion, so, blue and red light losses are — in principle — automatically corrected by the flux calibration routine.

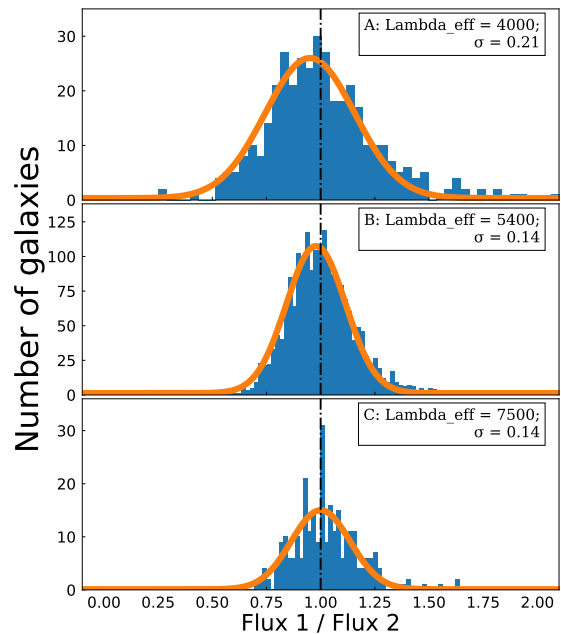


Figure 5. An estimate of the relative flux calibration error of the eBOSS spectra based on comparisons of repeat spectra of the same galaxies observed at two or more different epochs. Here we compare the sum the flux in a 200 \AA window centered at the wavelength, `LAMBDA_EFF`, that the spectrophotometric calibration is optimized for. For the majority of galaxies, this is 5400 \AA (Panel B), however most ELG targets have `LAMBDA_EFF`= 7500 \AA (Panel C) and most QSO targets classified as galaxies have `LAMBDA_EFF` = 4000 \AA (Panel A). The orange lines show Gaussian fits; the $1\text{-}\sigma$ spread of the data is listed in each plot. This represents the minimum uncertainty of a line flux measurement due to spectrophotometric calibration errors. These errors can be larger at wavelengths that are far from `LAMBDA_EFF` as shown in Figure 6.

In practice, this calibration approach works well: in the SDSS-I survey a flux calibration accuracy of $\sim 5\%$ was achieved at 4000 \AA ³. The main failure mode results from

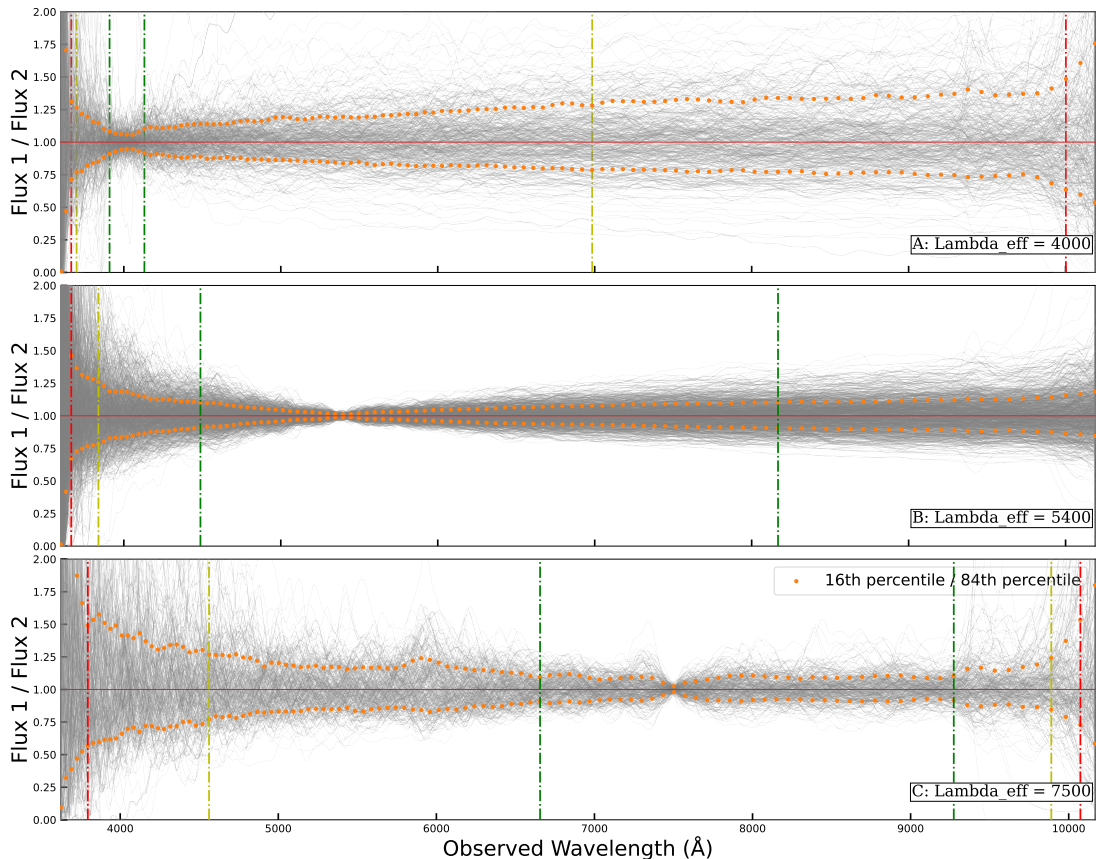


Figure 6. An analysis of the typical error in the spectral shape made by dividing pairs of repeat spectra after normalizing them at `LAMBDA_EFF`, the wavelength the flux calibration has been optimized for. We show galaxies with `LAMBDA_EFF` = 4000 Å, 5400 Å, and 7500 Å in panels A, B, and C, respectively. Each gray line represents a pair of spectra that were taken of the same galaxy in different epochs. Spectra in each pair were normalized at their respective `LAMBDA_EFF` and smoothed individually before computing their ratio. Small-scale wiggles in the gray lines are primarily due to the low S/N per pixel of the spectra. The 1σ spread of the data in 40-pixel-sized bins is shown as the orange dotted lines. Green, yellow, and red vertical lines have been added, marking where the percent error is 10%, 25%, and 50%, respectively. For most galaxies, spectrophotometric calibration errors will lead to line flux ratio errors < 25%. However, caution is advised when using emission lines observed near the blue and red ends of the spectrum.

the miscentering of objects in the fibers, which can occur due to the deformation of the aluminum plug plates, which are warped to match the curved focal plane of the telescope (D. G. York et al. 2000). For example, when the hole for an object fiber is centered too high (and the majority of the standards are centered correctly in their fibers), more blue light and less red light is captured by the object fiber than for the standards, leading to an error in the relative flux calibration. The SDSS-I and II surveys used 3" diameter fibers, which mitigated the fiber centering problems. For SDSS-III/IV (BOSS and eBOSS), the fibers were reduced to 2" in diameter to improve sky subtraction for the distant galaxies and quasars targeted. To evaluate the quality of the flux calibration in SDSS-IV/eBOSS, we take advantage of the large number of repeat galaxy spectra obtained.

In eBOSS, fibers were positioned on the plates to account for the expected atmospheric differential refraction, with different spectroscopic targets centered at different wavelengths in an attempt to mitigate light losses in particular parts of the spectrum. Most objects were centered on the position of 5400 Å light (1,716,144 spectra). However, objects targeted as QSOs were centered

around 4000 Å (23,870 spectra), while objects targeted as ELGs were centered at 7500 Å (161,820 spectra). This is reflected in the parameter `LAMBDA_EFF` found in the `spAll-v5_13_2.fits` file. To analyze the relative and absolute calibration for each unique `LAMBDA_EFF`, we selected pairs of galaxy spectra after applying a cut on median S/N per pixel. For `LAMBDA_EFF` = 4000 we used a $S/N \geq 3$ cut, resulting in 386 unique pairs. For `LAMBDA_EFF` = 5400 we used a $S/N \geq 6$ cut, resulting in 1094 unique pairs. Finally, for `LAMBDA_EFF` = 7500 we used a $S/N \geq 1.5$ cut, resulting in 279 unique pairs. The S/N cuts were implemented to reduce problematic negative pixels; the S/N thresholds are different for each `LAMBDA_EFF` to enable a reasonable number of pairs in each bin. In principle, these S/N cuts do not affect our analysis since the spectrophotometric quality is independent of S/N.

In Figure 5, we show the ratios of a 200 Å flux window centered at the `LAMBDA_EFF` in pairs of galaxy spectra. The pairs represent spectra of the same galaxy obtained at different epochs. In some cases, the same plate was observed on multiple dates; in others, the galaxies were targeted on two different plates with different sets of standards. The ratio of the galaxy fluxes at the `LAMBDA_EFF`

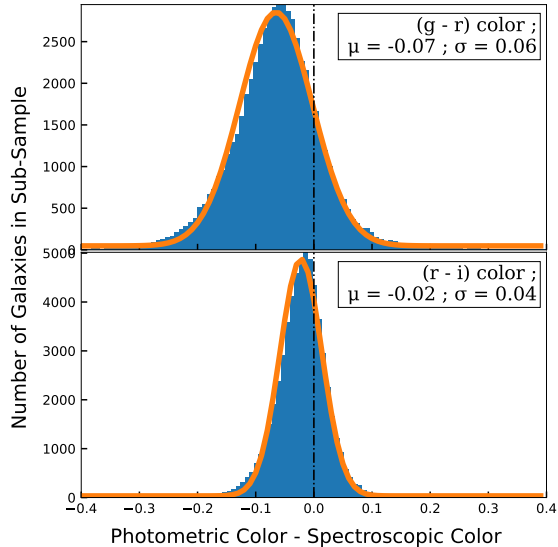


Figure 7. Comparisons of galaxy colors synthesized from the spectra with photometric colors for galaxies with $r < 17.7$ mag and spectra with `LAMBDA_EFF` = 5400 Å. This comparison measures the absolute calibration quality in eBOSS spectroscopy. Relatively bright galaxies are chosen for this comparison to minimize random error. In the **Top Panel** ($g-r$) colors are compared, whereas in the **Bottom Panel** ($r-i$) colors are compared. Lower σ values and μ values closer to zero indicate better absolute calibration.

provides a valuable assessment of the repeatability of the absolute flux calibration at this wavelength. A Gaussian fit to the distribution has a width of $\sigma = 0.21, 0.14, 0.14$ for `LAMBDA_EFF` = 4000, 5400, and 7500, respectively. Thus, for most eBOSS galaxies, the flux calibration is accurate to about 15-20% at wavelengths near `LAMBDA_EFF`.

In Figure 6, we explore the relative flux calibration of the spectra as a function of observed-frame wavelength for each `LAMBDA_EFF`. This is the error on the spectral *shape* that would impact emission line ratios widely separated in wavelength. Galaxy spectra are normalized at their `LAMBDA_EFF`, median smoothed by 100 pixels, followed by a 40-pixel average smooth, and then divided. The orange dotted line shows the $1-\sigma$ width of the distribution of all pairs in bins of 40 pixels.

According to Fig. 6, For `LAMBDA_EFF` = 4000 the relative flux calibration error is less than 10% between 3909 – 4208 Å, and less than 25% between 3733 – 7449 Å. The error is over 50% at wavelengths less than 3665 or greater than 10002 Å. For `LAMBDA_EFF` = 5400, the relative flux calibration error is less than 10% between 4488 – 8397 Å, and less than 25% between 3838 – 10283 Å. The error is over 50% at wavelengths less than 3665 or greater than 10283 Å. Finally, for `LAMBDA_EFF` = 7500, the relative flux calibration error is less than 10% between 6595 – 9273 Å, and less than 25% between 4562 – 9890 Å. The error is over 50% at wavelengths less than 3830 or greater than 10074 Å. These statistics suggest caution in using emission lines observed near the edge of the spectrum.

In Figure 7, we show the difference in color between the photometry and spectroscopy for galaxies with `LAMBDA_EFF` = 5400 Å and an r -band AB magnitude of

17.7 or smaller. The colors of the spectra have been synthesized using the SDSS filter curves (M. Fukugita et al. 1996). We compare synthetic photometry computed from the spectra (found in the `spAll` field `spectroflux`) to the observed photometry (`modelflux`). For this sample, $\sim 27.3\%$ of the galaxy’s light falls in the 2” fiber aperture, and thus we do not expect galaxy color gradients to impact our comparison significantly. At $r < 17.7$, the photometric errors on the $g-r$ and $r-i$ colors should be minor, and, as such, any deviations between the colors of the photometry and the spectroscopy likely indicate errors in the spectrophotometric calibration. Whereas Figure 6 demonstrates the consistency of the calibration, i.e., the precision, Figure 7 shows us the absolute calibration accuracy. In Figure 7, the further left the data lies, the more blue it is relative to the photometry. The $(g-r)$ color has a larger offset ($\mu = -0.07$) and standard deviation ($\sigma = 0.06$) than the $(r-i)$ color ($\mu = -0.02$; $\sigma = 0.04$). The difference in σ between the two colors is consistent with the larger spectrophotometric errors seen at blue wavelengths in the repeat spectra comparison (Fig. 6). The slight offset in $(g-r)$ color ($\mu = -0.07$ mag) implies that there are some minor systematic issues in the calibration, as previously found for SDSS-I ($\mu_{g-r} = 0.02$ mag)⁴. Similar analysis could not be performed on `LAMBDA_EFF` = 4000 and 7500 spectra, as there is not enough low-magnitude data available for these `LAMBDA_EFF`.

2.5. Known issues with the SDSS-IV data

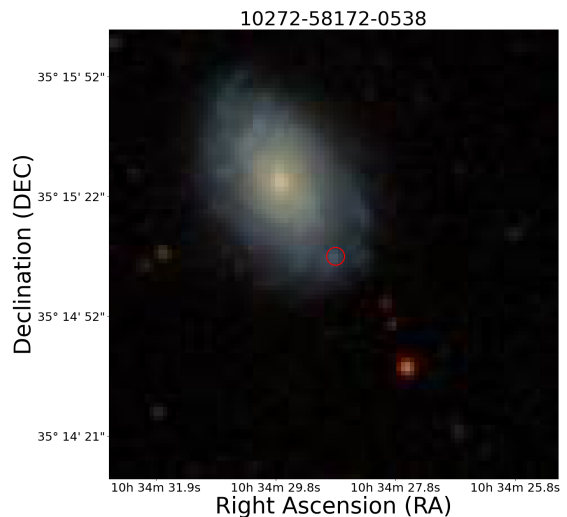


Figure 8. An example of a galaxy incorrectly deblended by the SDSS photometric pipeline. The H II region circled in red was considered a separate photometric object and targeted for spectroscopy as a quasar. (The circle represents the size of the eBOSS fiber.) The spectrum (Plate: 0272; MJD: 58172; Fiber: 0538) is classified as a galaxy and otherwise free of problems. However, quantities derived from the photometry will pertain only to the galaxy sub-region. For example, this object has a photometrically-derived stellar mass of $\log(M_*) = 5.2$ when it is clearly part of a much larger galaxy.

⁴ <https://classic.sdss.org/dr6/products/spectra/spectrophotometry.php>

There exist two caveats to our data resulting from known issues in SDSS-IV that we did not rectify. The first is that some large nearby galaxies are incorrectly deblended by the SDSS photometric pipeline, leading to incorrect photometric measurements. An example is shown in Figure 8, where an H II region has been incorrectly classified as a separate photometric object and selected for spectroscopy as a quasar target. The spectrum was subsequently classified as belonging to a galaxy; however, the galaxy’s stellar mass and other properties calculated from the photometry are incorrect. These deblending problems occur frequently enough at $z < 0.1$ to produce a substantial group of outliers in the eBOSS stellar mass–metallicity relation (i.e., galaxies with high metallicity and unrealistically low stellar masses; see Fig. 23). Objects with deblending issues are not straightforward to identify without visual inspection of the photometric images. A potential approach to finding such sources would be to determine whether an object lies within the Petrosian radius of another photometric object.

Our second caveat applies to galaxies with very high emission line EWs and low gas velocity dispersions (i.e., star-bursting dwarf galaxies). In the eBOSS spectra of these galaxies, the strongest emission lines such as [O III] 5008 and H α are sometimes clipped off. An example is shown in Figure 9. The missing portions of the emission lines typically have their inverse variance set to zero (i.e., they are flagged as bad data.) However, the lines are sometimes fit by the eBOSS-DAP if only the core of the line profile is flagged as bad; the accuracy of such fits is unclear.

The problem of clipped emission lines was well known in the SDSS-I; some code changes in DR7 improved, but did not eliminate, the issue (see §6.3 in K. N. Abazajian et al. 2009). The clipped lines arise from a combination of data reduction problems. One issue can be the saturation of the detector at the position of the brightest lines. Another issue can arise when the `spectro2D` data reduction pipeline combines the 3-12 individual spectroscopic exposures that make up the final spectrum. Slight mismatches between the exposures (due to small pointing differences, for example) cause the pixels associated with bright lines to be rejected because they differ by more than the errors allow between exposures.

The fully calibrated individual spectroscopic exposures are stored in the final FITS spectrum output by SDSS (the “full”, not the “lite” version). Custom software for combining these exposures could likely recover many of the clipped lines. However, this is beyond the scope of the current work. In some cases, clipped emission lines can be identified by looking for discrepancies between line EWs estimated by Gaussian fits vs. straight integration (see §4.2.1) or by flagging spectra with unusual line ratios (i.e., H α < H β). However, this method will not identify all cases of clipped lines, and therefore caution is advised in working with very low mass galaxies ($M_* < 10^8 M_\odot$) with high EW emission lines ($\text{EW}(\text{H}\beta) > 100 \text{ \AA}$).

3. METHODS

We aimed to produce a catalog of emission line fits, spectral indices, and stellar population template weights from the eBOSS galaxy spectra. To this end, we developed the eBOSS-DAP, an analysis pipeline built from the Mapping Nearby Galaxies at Apache Point Observatory - Data Analysis Pipeline (MaNGA-DAP) code package (K. B. Westfall et al. 2019; F. Belfiore et al. 2019). We begin by briefly describing the MaNGA-DAP in §3.1. In §3.2 and its subsections, we describe the modifications that we made to create the eBOSS-DAP. In §3.3 we provide an overview of the eBOSS-DAP workflow.

3.1. The MaNGA-DAP

The MaNGA-DAP is a multi-stage spectral fitting software tool designed to process and analyze the data collected by the MaNGA survey (K. Bundy et al. 2015). It handles the complex data cubes produced by the survey, which contain spatially resolved spectroscopy of nearby galaxies. The pipeline performs various tasks, including full-spectral fitting of the galaxy spectra to measure stellar kinematics and absorption-line indices from the stellar continuum and gas kinematics, fluxes, and equivalent widths (EWs) from Gaussian modeling of the emission lines. Within the MaNGA-DAP, stellar continuum fitting is done with the Python implementation of the Penalized PiXel-Fitting method (pPXF; M. Cappellari 2023) using a mix of template libraries and a multiplicative polynomial. The code follows a multistage process. First, the stellar kinematics are fit with the emission lines masked. Second, the stellar continuum and emission lines are fit simultaneously, with the stellar kinematics fixed to the result of the first step. Third, the best-fit emission-line model is subtracted from the galaxy spectra before measuring the absorption-line indices. Detailed algorithms for all modules in the MaNGA-DAP are described by K. B. Westfall et al. (2019, Sections 6-10) and F. Belfiore et al. (2019, Section 2). We use Version 4.3 of the MaNGA-DAP available on Github.⁵ The `examples/fit_one_spec.py` file from the MaNGA-DAP was adapted and used as the core component of the eBOSS-DAP pipeline.

We chose to base our code on the MaNGA-DAP for several reasons. The eBOSS and MaNGA datasets use the same spectrograph and have similar, but not identical, data structures (plates vs. cubes), allowing many methods to be used with minimal modification. We also chose the MaNGA-DAP for its modular capabilities. We were able to fully customize our template libraries, line lists, and spectral indices, as well as the data that is saved. Another boon is the ability of the MaNGA-DAP pipeline to run on many spectra simultaneously, significantly reducing computational time for our 1.9 million spectra. Another key feature is MaNGA-DAP’s ability to tie various emission line properties (line widths, velocity offsets, flux ratios) across multiple lines (F. Belfiore et al.

⁵ <https://github.com/sdss/mangadap>

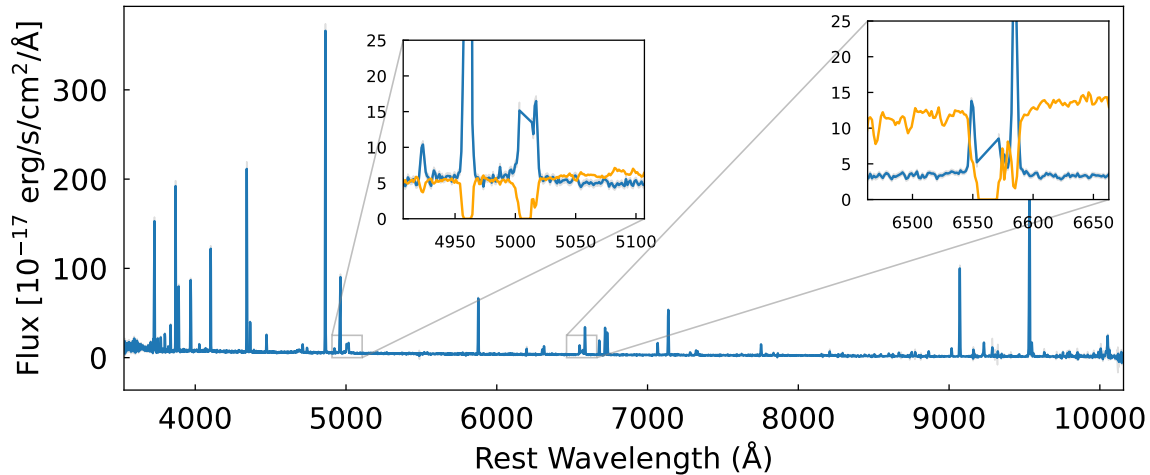


Figure 9. The spectrum (Plate: 11294; MJD: 58451; Fiber: 0164) for a galaxy with clipped emission lines. The spectrum is shown in blue, the error in light gray, and the inverse variance in orange. Two zoomed-in windows at [OIII] λ 5008 (left) and H α (right) have been added to demonstrate that the flux for these two lines has been masked out, as shown in orange, where the clipped lines coincide with an inverse variance of 0, which is a marker of bad data in SDSS. This effect is present in some galaxies with high EW emission lines and low gas velocity dispersions. See §2.5.

2019), using the implementation provided by pPXF. This allows us to use stronger lines to ensure robust fits for weaker lines by limiting some of their free parameters.

3.2. The eBOSS-DAP

To adapt the MaNGA-DAP for the goals of the eBOSS-DAP, we made several key changes to the code and supporting files, which fall into two classes: infrastructure changes and scientifically motivated changes.

Our first major infrastructure change was to enable the code to accept folders of one-dimensional spectra obtained on the same plate instead of single spectra or cubes. The details surrounding this change are found in §3.3. Additionally, we changed the preprocessing for the foreground Milky Way dust extinction correction. We use the `dustmaps` package (G. Green 2018) to retrieve the Milky Way E(B-V) value at the position of each target from the Corrected Schlegel, Finkbeiner & Davis (1998) dust maps (CSFD; Y.-K. Chiang 2023). We remove the foreground reddening from each spectrum using the `dust_extinction` code (K. D. Gordon 2024) with the K. D. Gordon et al. (2009) Milky Way dust attenuation law instead of the J. E. O’Donnell (1994) curve used for MaNGA.

An additional change was modifying the masking routine for the data, as eBOSS has slightly different mask bits than MaNGA. Our final set of infrastructure changes was fixing some minor issues we uncovered through our testing. For example, we found that if an emission line had only a few unmasked pixels, poor Gaussian fits could result. We, therefore, only report the results of the Gaussian fit for emission lines with less than 50% of their pixels masked out. We discuss the masking procedure further in §3.2.1. In addition, we only report spectral indices with less than 10% of their pixels masked out, as spectral indices are more sensitive to masking.

The first scientifically motivated change was to modify

the spectral template libraries that the code relies upon. The MaNGA-DAP is configured to be able to use several different stellar population template libraries (see discussion in Abdurro’uf et al. 2022a). These templates can be composed of individual stellar spectra or simple stellar population (SSP) models. We added a new SSP library called C3K that is discussed in detail in §3.2.2. We also made changes to the list of emission lines and line indices as detailed in §3.2.3 and §3.2.4.

3.2.1. Masking

The eBOSS data reduction pipeline creates a mask array that encodes data quality information differently from MaNGA.⁶ Accordingly, we had to implement our own masking routine. When fitting the data, we chose to use a combination of masks, primarily the AND_MASK⁷ and our own mask based on the inverse variance. The AND_MASK is a bitmask that flags pixels that were masked in every exposure contributing to the final spectrum; the bits encode the reason for masking. This mask was then trimmed down by removing certain bits that we found via visual inspection to be masking apparently good data, namely, bit 23: BRIGHTSKY, as well as bits 0-12, which are so-called FIBERMASK.BITS that mask the full spectrum. These bits are flagged when an error that would affect the full spectrum occurs, such as when the flat field is flagged as bad. There are 27,620 spectra or $\sim 1.5\%$ of our sample where a FIBERMASK.BIT is set. We chose to fit these spectra, but we add a column in the final output catalog containing the FIBERMASK.BITS. After masking the pixels identified in our trimmed mask, we added any pixels for which the inverse variance array was negative, infinite, or zero.

⁶ for further reference, see <https://www.sdss4.org/dr17/algorithms/bitmasks/>

⁷ The particulars of the AND_MASK are found here: <https://www.sdss4.org/dr17/algorithms/bitmasks/#SPPIXMASK>

In addition to masking pixels on *input* to the eBOSS-DAP, the analysis of the data leads to additional masking. The two primary masks indicate where the model is invalid (e.g., where the rest wavelengths of the template and galaxy spectra do not overlap) and which pixels in the galaxy spectra were rejected as outliers during the full-spectral fitting.

Our final additional mask consists of pixels in the window 3662 – 3706.3 Å and it is set only for stellar continuum and emission line fitting. This mask is created to avoid contamination of the continuum fit by high-order Balmer emission lines, which, as they are unfit by our code, pull up the continuum fit artificially. This mask is removed during spectral index measurement. The final mask is saved in the final output file for all spectra.

3.2.2. C3K Spectral Libraries

For our template library, we chose to generate SSPs and continuous star formation models based on the C3K stellar library (Conroy et al., in prep.) and MIST isochrones (A. Dotter 2016; J. Choi et al. 2016) found in the Flexible Stellar Population Synthesis (FSPS) package (C. Conroy et al. 2009; C. Conroy & J. E. Gunn 2010). The C3K model library, described in C. M. Byrne & E. R. Stanway (2023), consists of fully theoretical stellar spectra created using the ATLAS12 (F. Castelli 2005; R. L. Kurucz 1970) and SYNTHE (R. L. Kurucz 1993) codes. These models have stellar effective temperatures of $2500 \leq T_{eff} \leq 50,000$, surface gravities of $-1 \leq \log g \leq 5.5$ and metallicities $0.003 \leq \frac{Z}{Z_{\odot}} \leq 3.16$.

Approximately 80% of the eBOSS galaxy sample is at $z = 0.4 - 1.1$, which means that the blue edge of the spectrum is at restframe 1700 – 2600 Å. We chose to use the C3K SSPs primarily because most empirical models have limited UV coverage and/or low UV spectral resolution. Theoretical models also provide a denser exploration of parameter space (T_{eff} , $\log g$, Z), which can be important in achieving an optimal fit (P. R. T. Coelho et al. 2020). Additionally, the C3K models have higher spectral resolution than our data over most of the relevant wavelength range. Unlike observational data, they are unaffected by factors like flux calibration errors or sky subtraction residuals. Additionally, theoretical models are a better match to metallicities and stellar population age in high-resolution spectra (R. Asa’d et al. 2025). However, their precision is limited by the precision of the underlying atomic and molecular data, as well as the computational models used to generate them. (C. Conroy 2013; P. R. T. Coelho et al. 2020).

For our SSP model grid, we chose four metallicity bins and 18 age bins as seen in Figure 10. These ages were selected such that periods of rapid evolution received more finely binned SSPs to provide good coverage of different spectral shapes. Our youngest SSP model is 12.1 Myr old. To fit galaxies with on-going star formation we add two models that represent 5 and 10 Myr of continuous star formation. We adopted this approach to minimize the number of models needed. Because we are fitting

galaxy spectra, they are unlikely to have changes in their star formation histories on timescales shorter than 5 Myr.

We use FSPS to add nebular continuum to our continuous star formation models. (We did not add it to our SSPs because nebular continuum does not contribute significantly to stellar populations older than 10 Myr (N. Byler et al. 2017).) We found that for galaxies with high levels of on-going star formation nebular continuum is needed to properly fit the spectrum at 3600-3700 Å as seen in Figure 11. If nebular continuum flux is not present in the models, the continuum will be underestimated blue-ward of the Balmer jump (~ 3645 Å) while being overestimated red-ward. Additionally, this can cause loss of measured flux in [O II] $\lambda\lambda$ 3727, 3729, a critical emission line. A second concern is that, although the eBOSS-DAP does not measure Balmer lines bluer than H12, there is significant continuum infilling from high-order Balmer lines (H14→H30) as shown in Figure 11 panel **B**. If the nebular continuum is not added, all of this flux is inappropriately attributed to the continuum, and when the high-order Balmer line fluxes are added back into the continuum (by scaling the lines to H12), the model fit clearly overestimates the continuum.

The wavelengths of the C3K models natively span from 100 – 10^7 Å; however, for our models used in emission line fitting, we trimmed to 1281 – 10616 Å. The resolution of the C3K SSPs created by FSPS is $R \sim 1180$ between 1281 – 2750 Å, $R \sim 7060$ between 2750 – 9100 Å, and $R \sim 1180$ between 9100 - 10616 Å. For models used to fit the stellar continuum kinematics, we further restrict them to the $\lambda = 3000$ Å – 9000 Å range, with $R \sim 7060$. The spectral sampling of the C3K templates is also not uniform, meaning that we need to resample the spectra before the eBOSS-DAP can use them. To match the average sampling step across the wavelength range of our models, we resample the templates such that they are uniformly sampled in log space with a spectral spacing of $d \log \lambda = 7.239 \times 10^{-5}$ or 49.97 km s⁻¹. The templates are then resampled again by the DAP to match the wavelength array of each plate.

3.2.3. Emission Line Fitting

The MaNGA-DAP natively provides users with a flexible and modular file that details the emission line list. What sets this fitting routine apart is the ability to tie parameters of the lines, namely the flux, velocity, and velocity dispersion. Line tying (as described in K. B. Westfall et al. (2019) with features implemented in M. Cappellari (2012, 2023)) refers to requiring the parameters of two or more separate lines to be related to each other, for example: [OIII] λ 4960 flux = 0.331 [OIII] λ 5008 flux. More specifically, when tying the flux of two lines, one free parameter effectively governs the flux of both lines in the model, and the fitting algorithm adjusts that parameter to optimize the fit to both lines simultaneously. Table A1 stores the emission line information, including the ratios and the lines used for tying.

A new feature in eBOSS-DAP (which was possible but

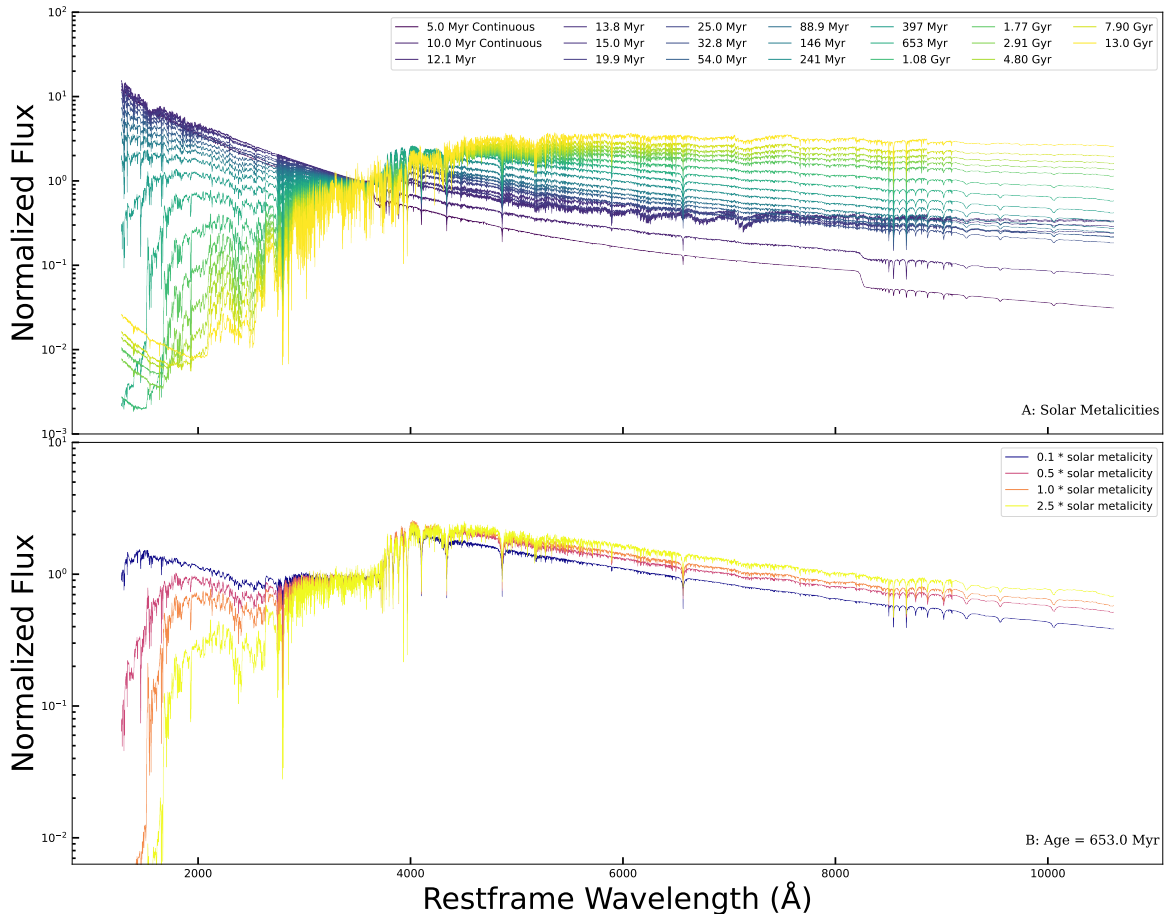


Figure 10. Stellar population templates employed by the eBOSS-DAP. The templates have been generated with FSPS (C. Conroy et al. 2009; C. Conroy & J. E. Gunn 2010) using the C3K stellar library (Conroy et al., in prep.). **Top:** Solar metallicity SSPs and two continuous models color-coded by age. **Bottom:** Four SSPs that share the same age of 653 Myr but vary in metallicity from $Z = 0.1 - 2.5 Z_{\odot}$. The full template library includes all ages shown at all four metallicities. This totals 80 templates. All templates are normalized to their flux at 3500 Å.

unused in previous MaNGA-DAP analysis) is the ability to specify that two line parameters be within some fractional range of each other. This can be seen with the example of [O III] $\lambda 5008$ in Table A1. Here, the line list specifies that the [O III] $\lambda 5008$ line must have equal velocity to $H\alpha$ (in the low redshift bin), but the velocity dispersion is free to be within 75% of the $H\alpha$ dispersion (i.e., $1/1.75 \sigma_{H\alpha} < \sigma_{[O III]} < 1.75 \sigma_{H\alpha}$). We chose to impose this velocity dispersion tie on all lines, as it helps weak lines to be fit accurately and does not have adverse consequences for the stronger lines.

The allowed range in dispersion ratios ($\sigma_{\text{line}} = 0.57 - 1.75 \sigma_{H\alpha}$) was selected after empirically testing the range of dispersion ratios found for strong emission lines when no velocity dispersion tie was used. It accommodates the wavelength-dependent instrumental resolution and allows for real physical differences between emission lines produced in different regions of a galaxy, for example, [O III] lines in the narrow line region of Type II AGN. Note that Type I AGN, which can have extreme velocity dispersion differences between Balmer and forbidden lines, are generally not included in our sample, as they are classified as quasars rather than galaxies by the SDSS `spectro1d` pipeline which measures redshifts and

spectral classifications.

The eBOSS-DAP makes several additions to the MaNGA-DAP emission line list provided by DR17 (K. B. Westfall et al. 2019; D. R. Law et al. 2021a). The list is increased to 78 lines, of which only 35 were fit in MaNGA. The 43 new eBOSS-DAP lines are demarcated by an asterisk in Column 1 of Table A1. These lines include all iron lines found in the line list and all lines of $\lambda < 3600$ Å. Of particular note are [Ne V] $\lambda\lambda 3347, 3427$ and [Fe X] $\lambda 6374$, which are used as AGN diagnostics. The bluest line we fit is [C III] $\lambda\lambda 1906, 1909$, which redshifts into the observed spectral range at $z = 0.87$.

Unlike MaNGA-DAP, which uses one line list for the entire sample, we use four distinct line lists that split our sample by $H\beta$ equivalent width (EW) and by redshift. This was done in an effort to resolve two major problems: data size and restframe wavelength coverage.

Initially, we were fitting all lines in all spectra, but we noticed that our weaker lines returned measurements consistent with noise in the majority of spectra. Therefore, we elected to split the sample into two subsamples: one with an $H\beta$ EW > 10 Å resulting in 167,466 spectra, and another with $H\beta$ EW < 10 Å resulting in 1,734,368 spectra. All lines were fit in the high EW

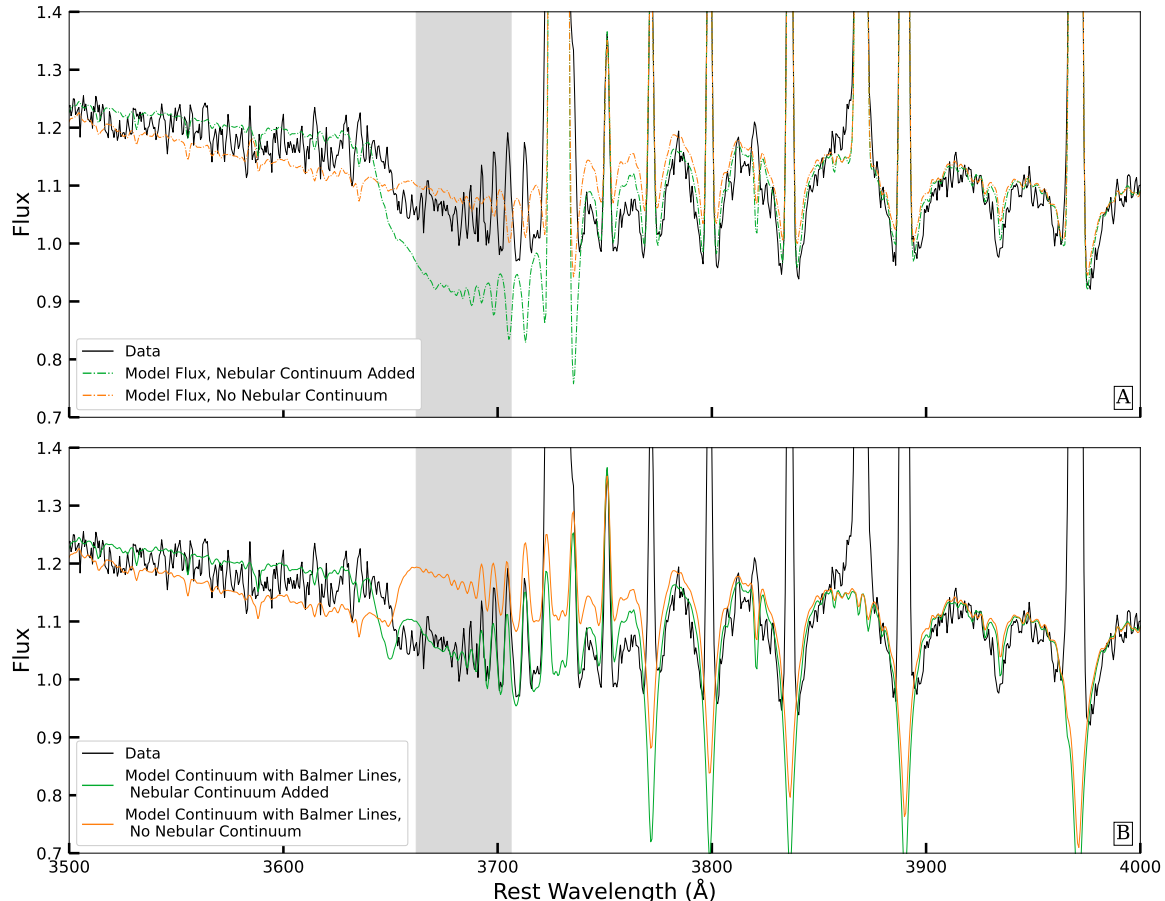


Figure 11. A comparison of stellar population models with and without nebular continuum. In both panels, the black line shows a stacked spectrum made from galaxies with very high $H\beta$ EW, the orange line is the best-fit stellar population model when templates that do not include nebular continuum emission are used, and the green line is the best-fit model with nebular continuum included. Additionally, a vertical gray band has been included to indicate the mask for the high-order Balmer lines at 3662–3706.3 Å. **Panel A:** The continuum from best-fit models for this stack. The models without nebular continuum (Orange line) underestimate the continuum blueward of 3662Å and overestimate it redward of 3706Å. The models with nebular continuum correctly estimate the continuum outside of the masked region. **Panel B:** Flux from high-order Balmer lines has been added to the continuum. This shows that, when the Balmer flux is included, all portions of the nebular continuum added models are better fits than models lacking the nebular continuum. The eBOSS-DAP does not fit these high-order Balmer lines; these models have been constructed by adding Balmer lines scaled to $H\alpha$ flux to the best fit continuum of the eBOSS-DAP in both the no nebular continuum and the added nebular continuum case.

subsample, but in the low EW sample, a 27-line subset, made up of typically stronger lines, is fit. These lines are flagged in the last column of Table A1.

Our second division is a result of the wide redshift range of our data. A practical limitation of the MaNGA-DAP is that it must designate a reference line when setting up the set of tied emission lines. The line chosen is effectively irrelevant to the optimization algorithm, but the tying setup fails if the reference line is outside of the observed spectral range. This means that, while we may like to tie all of our lines to $H\alpha$, if it is outside of our observable window, all lines tied to it are not fit, regardless of whether the tied lines are observable. To remedy this, we made a redshift cut, and for all spectra above $z = 0.4963$, we tied lines to $H\beta$ instead. We chose this redshift cut as this is when $H\alpha$ enters a zone of increased measurement error near the edge of the spectrum, as seen in Figure 6. Roughly 60% of our sample lies above this redshift threshold, drastically increasing the quantity of data we can successfully process.

3.2.4. Spectral Indices

Following K. B. Westfall et al. (2019), we adopt the term “Spectral Index” to refer to measurements of stellar continuum features. We have not changed any details of the spectral index measurements or outputs as specified in Table 4 of K. B. Westfall et al. (2019) and Section 5.2.2 of Abdurro’uf et al. (2022b). Our singular contribution is the addition of a “BalmerBreak” index. We adopt the definition of B. Wang et al. (2024), which is measured identically to D4000 but with a blue bandpass of $\lambda = 3620.0 - 3720.0$ Å and a red bandpass of $\lambda = 4000.0 - 4100.0$ Å in vacuum wavelengths. This additional index allows us to measure the Balmer break, which appears as a discontinuity or “jump” in the stellar continuum spectrum at around 3645 Å. This break is caused by the ionization of hydrogen atoms from the second energy level within stellar atmospheres, leading to a drop in intensity at wavelengths shorter than this limit. The Balmer break is prominent in SSPs with ages of 0.3 - 1 Gyr, and it is therefore used in estimating the

age of stellar populations and inferring the star formation history of galaxies.

3.3. Workflow

Running the eBOSS-DAP first requires a few setup steps. For each galaxy, we collect the foreground Milky Way $E(B-V)$ value from the CSFD (Y.-K. Chiang 2023) maps in the `dustmaps` (G. Green 2018) package and the galaxy redshift from the `spAll-v5_13_2` file released in DR17. The sample is then divided into “low- z ” and “high- z ” samples, distinguished by those galaxies below and above $z = 0.4963$, respectively. Galaxies in the low- z bin tie all emission lines to $H\alpha$, whereas the high- z samples use $H\beta$; recall, this is largely a practical matter dictated by the use of the DAP. We also divide the sample into “low-EW” and “high-EW” samples based on a preliminary measurement (using the DAP) of the $H\beta$ EW being below or above 10 \AA , respectively. All emission lines are fit for galaxy spectra in the high-EW sample, whereas only a subset of the strongest lines are fit to the low-EW sample; see Table A1. The division by z and EW leads to four samples of spectra to be fit.

Spectra in each sample are fit in groups based on their plate number. This grouping is also primarily a practical issue: Each spectrum is treated independently, but this grouping allows us to perform common preparation steps (like building the spectral template library) once for a large number of spectra, instead of once per spectrum. The detailed steps performed for each spectral group (which closely follow the steps for the MaNGA DAP described by K. B. Westfall et al. 2019) are as follows:

(1) The spectral templates are resampled to the pixel scale of the galaxy data divided by an integer, N . Here we choose $N=4$ such that the line-spread function of the C3K templates (see §3.2.2) is still well-sampled. Due to C3K’s varying spectral resolution, two spectral libraries are created. The first has coverage of $\lambda = 1280 \text{ \AA} - 10600 \text{ \AA}$ ($R \sim 1180 - 7060$) and is used to measure the stellar continuum and emission lines. The second has coverage of $\lambda = 3000 \text{ \AA} - 9000 \text{ \AA}$ ($R \sim 7060$) and is used to measure the stellar kinematics.

(2) The galaxy spectra are packaged into two-dimensional arrays with a common wavelength vector by adding modest zero-padding. The padded spectral regions are included in the masks (see Section 3.2.1). The observed fluxes and uncertainties are corrected for Milky Way extinction using the $E(B-V)$ values and the `dust_extinction` (K. D. Gordon 2024) package using the K. D. Gordon et al. (2009) Milky Way extinction law. Masks from §3.2.1 are applied.

(3) The stellar kinematics are measured for each spectrum independently using pPXF (M. Cappellari 2023). The emission lines are masked during this fit, and we use an eighth-order polynomial in (additive) combination with the spectral templates with the shorter spectral range to model the continuum. See K. B. Westfall et al.

(2019), Section 7.⁸

(4) The emission-line properties (flux, velocity, and velocity dispersion) are modeled simultaneously with the continuum templates, where the stellar kinematics are fixed to the results from the previous step. The continuum templates used include nebular continuum emission in the two continuous models as discussed in §3.2.2. For this module, the continuum templates used are those with the longer wavelength range, and we include an eighth-order *multiplicative* polynomial to apply low-order continuum modifications to address attenuation. Additionally, this polynomial helps minimize issues related to flux-calibration errors/difference between the template library and the data. The best-fitting model Gaussian profiles for each emission line are then used to calculate their equivalent widths. The continuum for the EW measurements is defined by a line connecting the median flux in two passbands (red and blue, as defined in the input file) to the (unweighted) center of each passband. The continuum level used in the EW calculation is the value of this line at the fitted center of the emission line.

(5) In addition to the emission-line properties measured from the best-fitting Gaussian function, we also measure emission-line fluxes and EWs by direct integration of the continuum-subtracted spectrum. The code utilizes two sidebands to normalize any deviations from the continuum by drawing a line that passes through the coordinates defined by the center of each passband and the median flux within the passband. The continuum value is taken as the value of that line at the (measured) emission-line center. See K. B. Westfall et al. (2019), Section 9, and F. Belfiore et al. (2019) for further details. We only report the EW measurements, which are primarily used as a fit-quality metric; i.e., the EWs measured using the best-fit Gaussian and direct integration should be statistically identical for high-quality fits (see §4.2.1).

(6) The last analysis step is to measure the set of spectral indices described in §3.2.4 for our eBOSS spectra, after first subtracting the best-fit emission-line-only model. See K. B. Westfall et al. (2019), Section 10, and Abdurro’uf et al. (2022a), Section 5.2.2.

(7) Finally, the analysis results are saved to a FITS file, one file per spectrum. Additionally, all non-detections and failures have both the signal and error overwritten with -999.0, the eBOSS-DAP error code. Once the analysis of all spectra is complete, the individual output files are aggregated into our final output catalogs; see Section 4.1.

4. RESULTS

We ran the eBOSS-DAP on a sample of 1,901,834 galaxy spectra with 1,899,553 successfully passing the full pipeline, giving us a 99.88% success

⁸ Measurements of the stellar velocity dispersion that exceed 350 km s^{-1} are considered erroneous. The output database replaces such measurements by imposing this upper limit, setting $\sigma_* = 350 \text{ km s}^{-1}$.

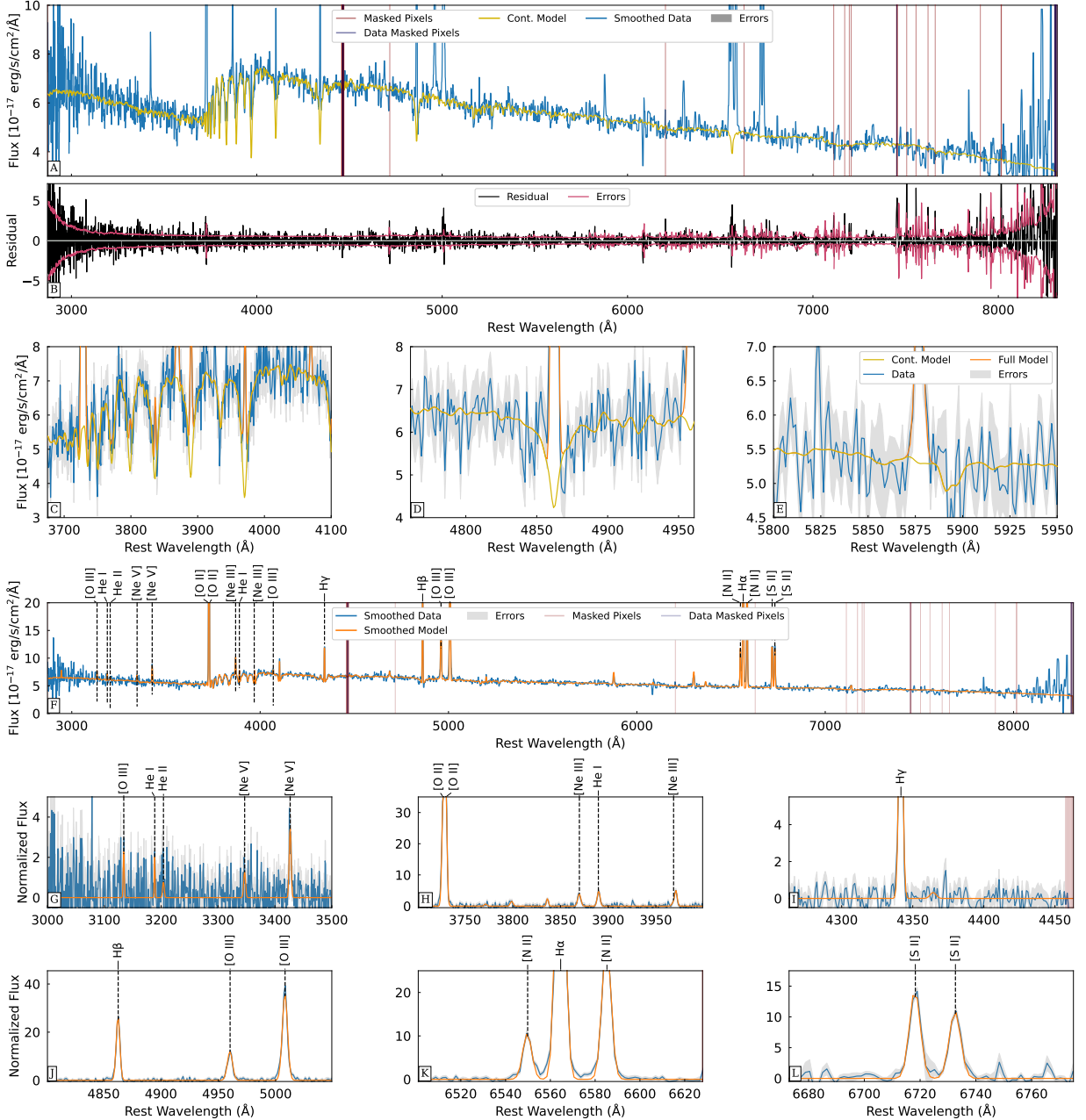


Figure 12. Sample eBOSS-DAP fit for the spectrum spec-4037-55631-0920.fits, which was categorized as an AGN using the Baldwin, Phillips, and Terlevich (BPT) (J. A. Baldwin et al. 1981) diagnostic. In all panels, the processed data are shown in blue. The best-fit continuum model is shown in dark yellow. The full best-fit model, including emission lines, is shown in orange. The masked portions are shown as vertical red bars. Errors are shown in gray bands. **Panel A:** A zoomed-in view on the smoothed continuum to demonstrate the quality of the fit. **Panel B:** The residual of the full model fit (black). There is a white line at zero for legibility and a red line showing the errors on the residual. **Panels C, D, and E:** Zoomed-in windows showing the continuum fit near some strong stellar absorption lines: the low-order Balmer lines (C), $H\beta$ (D), and Na I (E). **Panel F:** The full fit (stellar continuum plus emission lines) compared to the data. Emission lines are labeled. **Panels G-L:** Various zoomed-in locations of important emission lines, which have been labeled. These panels are continuum-subtracted, so the continuum flux is zero at all points.

rate. Figure 12 shows an example of the eBOSS-DAP’s continuum and emission line fits. Two additional spectra are shown in the Appendix (Fig. C1, Fig. C2).⁹ Panels A – E showcase the quality of our continuum fits, zooming in on some important spectral features.

⁹ These plots are not generated as part of the eBOSS-DAP; they are generated by a separate program found here: <https://github.com/owenmatthewsa/ebossdap/>

Similarly, panels F – L zoom in on several important emission lines and show that our line fitting is robust.

In §4.1 we discuss the catalogs generated by the eBOSS-DAP. In §4.2, we assess the quality of the catalog data by comparing measurements made on duplicate spectra and comparing to some existing catalogs in the literature. Finally, in §4.3, we present a series of plots that further characterize the eBOSS sample and illus-

trate its scientific potential.

4.1. Catalogs

We use the eBOSS-DAP outputs to create two emission line catalogs: one for the full sample (eBOSS-DAP_emlines_full_v#.fit; 1,899,553 spectra, which utilizes the reduced emission line list (27 lines), and one for the high equivalent width ($H\beta$ EW $> 10 \text{ \AA}$) sample (eBOSS-DAP_emlines_high_ew_v#.fit; 167,466 spectra), which makes use of the full line list (78 lines). The column descriptions of these catalogs are found in Table B1. All emission lines are corrected for foreground Milky Way reddening as described in Step (2) in §3.3. Notably, we include, along with the emission line velocity dispersions, the instrumental dispersion corrections; however, we do not implement these corrections, as there are cases where the instrumental resolution is larger than the measured line width, which can lead to potential errors. This is consistent with the treatment of these values in MaNGA and can be remedied by the methods illustrated in S. Chattopadhyay et al. (2024) and D. R. Law et al. (2021b).

The final catalog is a catalog of the spectral indices and the stellar population template weights (eBOSS-DAP_spind_full_v#.fit). The SPIND extension contains the spectral index catalog and the column descriptions given in Table B2. To find the units of a particular spectral index, readers should refer to the table of spectral indices (Table 4) in K. B. Westfall et al. (2019). These spectral indices are not corrected to a fixed velocity dispersion, as they were in the MaNGA-DAP; however, the corrections are included in the catalog if needed. The TPLWGT extension contains the template grid weights as well as the multiplicative polynomial values required to produce the model as described in Table B3.

To help visualize the eBOSS-DAP catalog, we have produced the following two figures. In Figure 13 we show a set of S/N histograms for our Gaussian fits to 12 commonly-used emission lines in our catalog, annotated with the number of detections of $S/N > 5$ in each line. Of note is the large quantity of galaxies with $[\text{Ne V}]$ $S/N > 5$. We will explore these objects further in future work (Matthews Acuña et al., in prep.).

In Figure 14 we show a histogram of the errors in four popular spectral indices. Due to the way spectral indices are measured, values may be positive or negative. S/N measurements are misleading when the index values approach zero, so we elected to simply show the errors in these indices. We additionally include the number of spectra in D_n4000 and $H\delta_A$ which pass the quality cuts suggested in G. Kauffmann et al. (2003) of D_n4000 error < 0.03 and $H\delta_A$ error < 0.8 .

4.2. Data Quality Assessment

We will assess data quality in three ways: Comparing Gaussian and direct integrated EWs (§4.2.1), comparing eBOSS-DAP data with SDSS pipeline emission line mea-

surements (§4.2.2), and comparing measurements made on repeat spectra (§4.2.3).

4.2.1. Gaussian vs Integrated EW Comparisons

We test the integrity of our Gaussian emission line fits by comparing the emission line equivalent widths (EWs) computed from the Gaussian fits to those found by integrating the continuum-subtracted spectrum between the line boundaries specified in Table B1. These integrated EWs should be within a standard deviation of the Gaussian EWs found by the model fitting and, as such, offer a check on the quality of any particular fit. Following F. Belfiore et al. (2019), we compare the Gaussian and integrated EWs by computing their percent difference as a function of S/N.

In Figure 15 we see that as S/N increases, the integrated and Gaussian EWs grow closer, as expected. Of note is that both $H\alpha$ and $[\text{S II}]$ have, on average, lower integrated EWs. This is caused by the narrow integration boundaries used for these lines due to the presence of nearby lines (see Table B1). In most of the lines, the Gaussian and integrated EWs agree within the expected margin of error, with slightly higher deviations in $H\alpha$ and $[\text{S II}]$, likely caused by broader components outside of the integration bounds of those lines. Additionally, the $[\text{O III}]$ and $H\beta$ lines show higher than expected deviations, likely due to substructure that is not well fit by a Gaussian – for example, a low-level broad component. Both Gaussian and integrated EWs are included in the eBOSS-DAP catalogs.

4.2.2. SDSS measurement Comparisons

SDSS provides an emission line catalog for the eBOSS sample stored in the spZline files.¹⁰ However, there are several issues with the SDSS spZline catalog that motivated the development of the eBOSS-DAP: the SDSS line list comprises only 28 lines compared to our 78; the emission lines are not corrected for Milky Way dust attenuation; and stellar absorption indices are not measured. Moreover, there is only minimal documentation available on the methods used to create the spZline catalog (A. S. Bolton et al. 2012). Nonetheless, it provides a valuable point of comparison for the eBOSS-DAP catalog.

To compare the two sets of emission line measurements, we first corrected the spZline measurements for Milky Way dust attenuation using the same process as the eBOSS-DAP. We then plot the flux of an emission line found by the eBOSS-DAP divided by the flux in the spZline catalog and compare it to the S/N of that line, as shown in Figure 16. Random variations are expected to produce a shape in which the standard deviation at any S/N is given by $\sigma \simeq \frac{\sqrt{2}}{S/N}$. In Figure 16, we compare the strong optical emission line fluxes of $[\text{O II}]$ 3726,3729, $H\beta$, $[\text{O III}]$ 5008, $H\alpha$ and $[\text{N II}]$ 6584, and $[\text{S II}]$ 6718,6733.

¹⁰ https://data.sdss.org/datamodel/files/BOSS_SPECTRO_REDUX/RUN2D/PLATE4/RUN1D/spZline.html

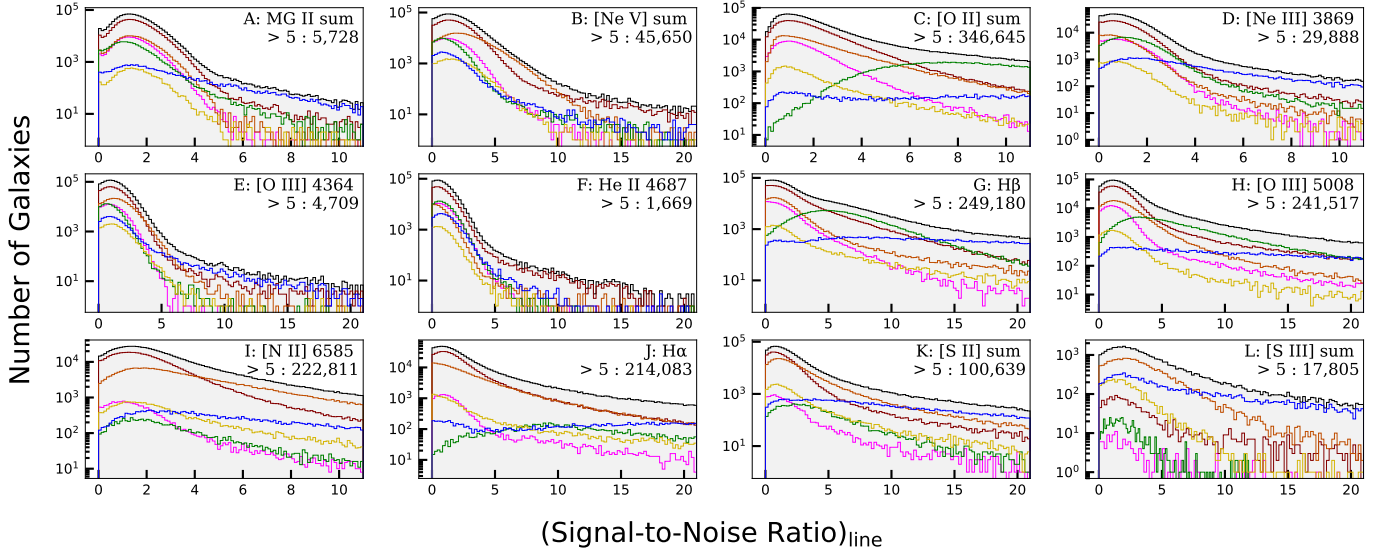


Figure 13. The S/N histograms of 12 lines in the eBOSS-DAP full sample, split by target classification. The target classes are color-coded identically to Fig. 1. Additionally, the number of galaxies that have $S/N > 5$ in the line flux has been included underneath the line name.

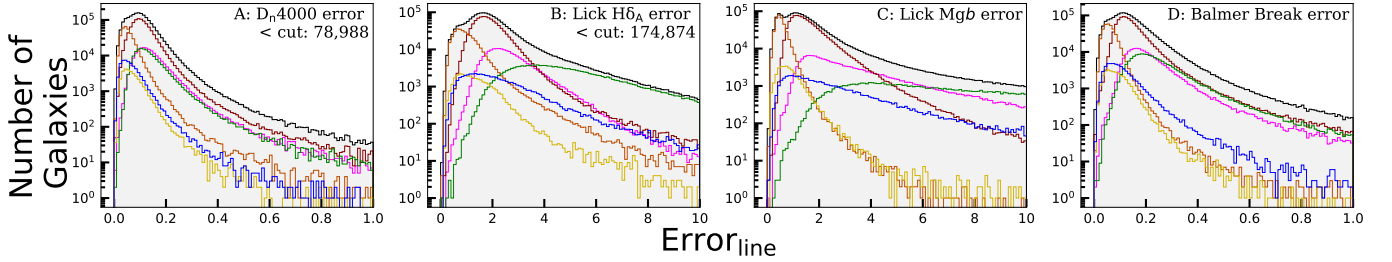


Figure 14. Histograms of the errors in four spectral indices in our full sample, split by target classification (see Fig 1 for color coding). Additionally, the number of galaxies that pass the quality cuts suggested by G. Kauffmann et al. (2003) are included underneath the index name for D_n4000 and $H\delta_A$ (see §4.3.5 for descriptions of these cuts).

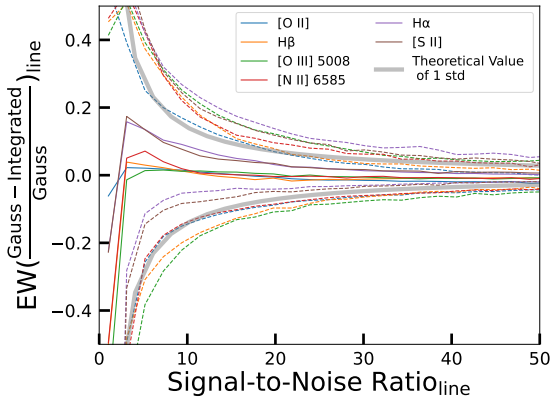


Figure 15. A comparison of Gaussian and integrated equivalent widths (EWs) relative to S/N for six commonly used strong emission lines. We take the Gaussian EW, subtract the integrated EW, and divide the result by the Gaussian EW to find the percent difference. Solid lines represent the median, while the dashed lines represent the standard deviation. A gray line has been included to show the expected value of the standard deviation given the S/N.

For most lines, the standard deviation of the flux measurements (pink points) decreases with S/N as predicted (orange lines), demonstrating the expected level of agreement between the eBOSS-DAP and the `spZline` catalog.

$H\beta$ shows the most prominent difference in the two line flux measurements, being 0.128 dex higher on average in

the eBOSS-DAP. This can be attributed to the fact that $H\beta$ lies in a strong stellar absorption feature, which is modeled differently in the two codes. The SDSS code uses a Principal Component Analysis (PCA) approach and the ELODIE empirical stellar library (P. Prugniel & C. Soubiran 2001) to fit the stellar continuum (A. S. Bolton et al. 2012). The ELODIE library is known to be incomplete, especially for very hot stars and at non-solar metallicities (C. Maraston & G. Strömbäck 2011). In addition, PCA spectral reconstruction can sometimes produce non-physical spectra since the eigenvectors summed to create the final spectrum can be added or subtracted. Thus, it is likely that the eBOSS-DAP, with its non-negative combination of modern stellar population synthesis models (see §3.2.2), provides an improved stellar continuum fit and a more accurate $H\beta$ flux.

Additionally, $H\alpha$ shows a slight negative preference in the low S/N regime, while $[N II] 6585$ shows a slight positive preference. This is likely due to SDSS assigning flux from $H\alpha$ to $[N II] 6585$ in low S/N data. $[S II] 6718,6733$ also has a slight positive preference, meaning that the eBOSS-DAP assigned it more flux in low S/N data than SDSS did.

4.2.3. Repeat Spectra Comparisons

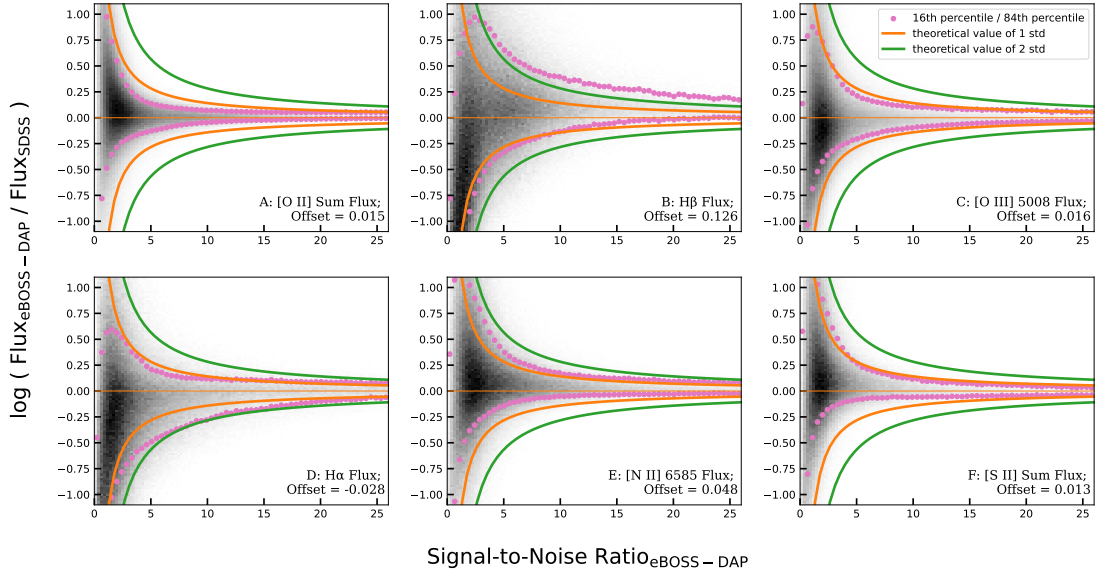


Figure 16. A comparison of line flux measurements in the eBOSS-DAP and the SDSS `spZLine` catalog for six relatively strong emission lines. The y-axis shows the log of the ratio between the flux from the eBOSS-DAP and the dust-corrected SDSS-provided measurement for the same object for a particular line. The x-axis plots the S/N of that observation in the eBOSS-DAP. The 1-sigma spread of the data is plotted in pink points, which can be visually compared to the expected value at a specific S/N, shown in orange and green lines at the 1-sigma and 2-sigma levels, respectively. The average offset for lines with $\text{S/N} > 3$ has been given for each line in the lower right of each panel.

Our final quality assessment was to make use of the 197,521 repeat spectra that eBOSS took to test consistency in measurements. In Figures 17 and 18 we plot the flux (or equivalent width) of an emission line divided by its value in a repeat observation and compare this ratio to the average S/N of the two observations. In Figure 17, we show the strong optical emission line fluxes of [O II] 3726,3729, H β , [O III] 5008, H α and [N II] 6584. The standard deviation of the repeat data (pink points) decreases with S/N as predicted (orange lines), but shows some deviations at high S/N. This is due to variations in the spectrophotometric calibration between the repeat spectra (see §2.4.) Both statistical error and variations in spectrophotometric calibration drive differences in the fluxes measured in repeat spectra. In the low S/N regime, emission line differences are dominated by statistical error, which is well captured by the eBOSS-DAP (the pink 1- σ values of the data line up well with the orange theoretical lines). However, in the high S/N regime, the spectrophotometry errors become dominant, and then the difference between the repeat spectra becomes larger than our measured errors (the pink 1- σ values of the data lie outside the orange theoretical lines). Notably, equivalent widths are free from spectrophotometry errors. Consequently, the H β EW differences (Panel C) show improved agreement of the pink points and orange lines at high S/N, although the errors are still slightly underestimated.

In Figure 18, we show a comparison of the fluxes from repeat spectra of three intrinsically weak emission lines: [Ne V] 3426, [O III] 4364, and He II 4687. These lines are only detected at $\text{S/N} > 5$ in $\sim 1\%$ of the galaxies with repeat spectra, making our comparison statistics more marginal. Nonetheless, we observe some differences from

Figure 17: for [Ne V] (and to a lesser extent [O III] 4364) at $\text{S/N} \simeq 2 - 6$ the pink points deviate from the orange lines, suggesting that the measured error of the line fluxes substantially underestimates the true error. Errors in the continuum fit can impact low EW lines such as these; however, the eBOSS-DAP fits the continuum simultaneously with the emission lines, and therefore, the associated error is included in the flux errors. Therefore, this is unlikely to be the source of the discrepancy. Notably, the strong emission lines in Fig. 17 show reasonable agreement between the predicted and actual errors at $\text{S/N} = 2 - 6$. For these weak lines, we suspect that rare spurious detections may outnumber real line detections in this S/N regime. The wavelength of [Ne V] 3426 also means that the line is commonly observed at the blue edge of the spectrograph, where the spectrophotometry errors are substantial (see §2.4). Users of the catalog are advised to exercise caution when conducting science with these and other weak lines and to utilize repeat spectra to better understand the appropriate detection threshold.

Unfortunately, it is not possible to accurately report the spectrophotometry error for an individual line flux measurement, as this depends on a complex interplay of plate drilling errors, telescope guiding errors, the airmass and seeing at the time of observation, errors in spectral typing the standard stars on the plate, etc. However, we used the repeat spectra to compute a scale factor that can be applied to the reported uncertainty of each line to approximately account for the additional uncertainty arising from spectrophotometric errors. These values are computed from the ratio of the measured errors to the 1- σ dispersion of the repeat spectra (e.g., the ratio of the pink points to the orange lines) for emission lines with $\text{S/N} > 3$. In Table 1, we list this recommended scale

factor for some commonly used emission lines. We also report the scaling that should be applied to the errors of various common line ratios. These correction factors have lower values than for the line fluxes because they are only sensitive to changes in the shape of the spectrum rather than its zero-point. Readers are referred to §2.4 for additional details on the spectrophotometric calibration.

Table 1
Uncertainty Scaling

Name	Recommended Uncertainty Scaling
[O II]	0.099
[Ne III] 3869	0.122
H β	0.148
[O III] 4364	0.147
[O III] 4960	0.141
[O III] 5008	0.141
[O I] 6302	0.124
He I 5877	0.12
H α	0.183
[N II] 6585	0.16
[S II] 6718	0.162
[S II] 6732	0.154
[Ne V] 3347	0.033
[Ne V] 3427	0.047
He II 4687	0.164
σ_*^1	1.28
R3	0.059
O23	0.076
N2	0.064
H α /H β	0.079

Note: these values are added in quadrature with the errors on those values. The values for the scaling were found by fitting the equation

$$\sigma_{\text{measured}} = \sqrt{(\sqrt{2}/(S/N))^2 + (\sqrt{2} * a)^2},$$

where a is the value shown in this table. The uncertainty scaling on σ_* , is multiplied rather than added and is fit by $\sigma_{\text{measured}} = \sqrt{2}/(S/N) * a$.

Our final validation step was to assess the quality of our stellar continuum kinematics, in particular the stellar velocity dispersion σ_* , by comparing measurements made from repeat spectra. Figure 20 shows that the reported kinematic errors explain the variation in the pairs with high precision, requiring only a scaling of 1.28 on the error, which is less than that of any individual line. The stellar velocity dispersion is measured with an error of less than 50 km s^{-1} for 82.5% of the sample.

4.3. Sample Characterization

As part of this investigation, we have made a slate of figures of the data to provide a clear picture of the make-up of the eBOSS-DAP catalog and illustrate the catalog’s possible uses: a mass–stellar velocity dispersion diagram, a BPT diagram, a star formation rate (SFR) vs stellar mass diagram, a mass–metallicity diagram, and a $H\delta_A$ vs Dn4000 diagram.

The stellar masses are from a catalog of SED-derived parameters produced by D. Miller et al., in prep, using

the Code for Investigating GALaxy Emission (CIGALE; M. Boquien et al. 2019). The inputs to the SED fitting are the SDSS redshift, the Legacy Survey *gri* photometry (A. Dey et al. 2019), the WISE (E. L. Wright et al. 2010) W1-W3 band photometry and the Dn4000 index measured by the eBOSS-DAP. The SEDs were computed by using a grid of parametric star-formation histories (a delayed τ model plus a burst), G. Bruzual & S. Charlot (2003) SSP models with a Chabrier IMF (G. Chabrier 2003), nebular emission, a D. Calzetti et al. (2000) dust attenuation law, and a B. T. Draine et al. (2014) dust emission law. Typical errors on the stellar masses are ± 0.07 dex.

4.3.1. Mass- σ_*

In Figure 20 we show a plot of the stellar continuum velocity dispersion measured by the eBOSS-DAP versus stellar mass, M_* , measured from the photometry with CIGALE (D. Miller et al, in prep.). The eBOSS-DAP measurements of stellar kinematics include 248,467 more $S/N > 5$ measurements than the SDSS pipeline stellar kinematics (A. S. Bolton et al. 2012), totaling 1,216,779 measurements, or 64% of the sample. Included in Figure 20 are best-fit lines to the $0.6 < z < 0.7$ Smithsonian Hectospec Lensing Survey (SHELS; M. J. Geller et al. 2005, 2014, 2016) sample and the $0.02 < z < 0.2$ SDSS main galaxy sample (M. A. Strauss et al. 2002) found by H. J. Zahid et al. (2016). The median relation for eBOSS is shown as a white line over the same mass range as these two samples ($9.0 < \text{Log}(\frac{M_*}{M_\odot}) < 11.5$). Our data, which peaks at $z \simeq 0.55$, has broad agreement with both the low- z SDSS sample and the higher redshift SHELS sample.

4.3.2. BPT

Our next example figure is the Baldwin, Phillips, and Terlevich (BPT) diagram (J. A. Baldwin et al. 1981) using the updated classification lines from D. R. Law et al. (2021c). The BPT uses a combination of $\log(\frac{[\text{O III}] 5008}{\text{H}\beta})$ (R3) and $\log(\frac{[\text{N II}] 6584}{\text{H}\alpha})$ (N2) to identify the origin of emission lines in galaxies. It is typically understood that N2 acts as a proxy for metallicity and R3 acts as a proxy for ionization level. Star-Forming Galaxies (SFGs) span a broad range of metallicity and ionization parameter, but the two are generally anti-correlated; e.g., high metallicity galaxies have low ionization parameter (X. Ji & R. Yan 2022).

AGN are typically found in massive metal-rich galaxies, and they can be a powerful source of hard ionizing photons, leading to high ionization parameters. Thus, the presence of an AGN will increase the R3 ratio as hard ionization from AGN will increase [OIII] (L. J. Kewley et al. 2013). Additionally, as AGN emission lines trace the Narrow Line Region (NLR) rather than interstellar medium (ISM) gas, [N II] emission will be much higher in AGN than in SFGs. This is because the NLR is far denser and hotter than the gas in the ISM, leading to much more

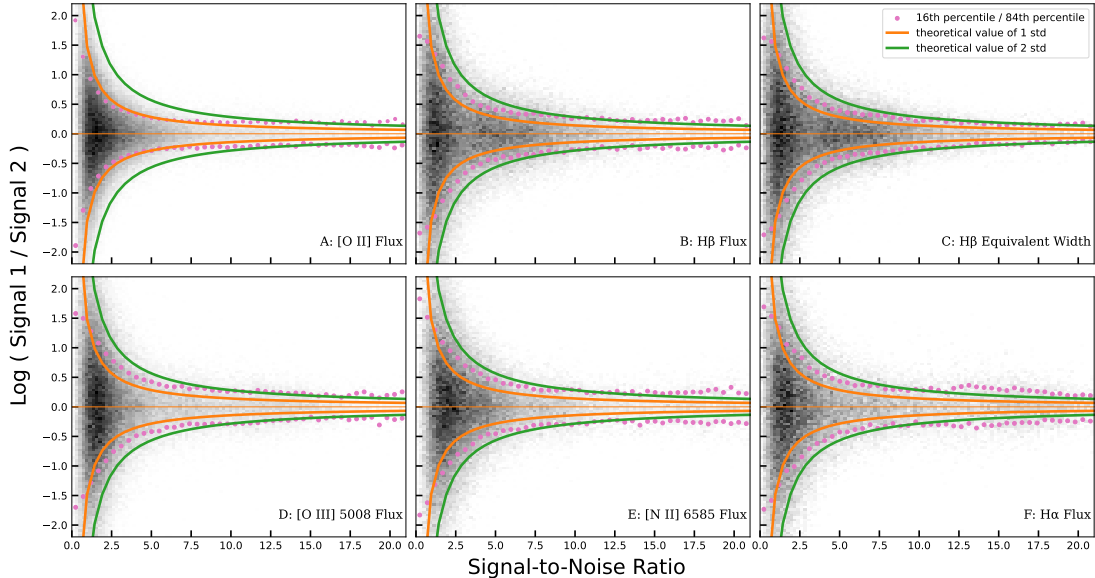


Figure 17. A comparison of line fluxes and EWs measured by the eBOSS-DAP in repeat galaxy spectra as a function of the emission line S/N. The data are shown in grayscale; pink dots show the 1- σ width of the distribution. Orange and green lines show the expected 1- σ and 2- σ spread of the data given the line S/N. Good agreement between the pink points and orange lines indicates that the errors on the emission line measurements are correct. **Panels A, B, D - F:** These panels compare fluxes of five relatively strong emission lines. At high S/N errors on the lines appear to be underestimated; this is a consequence of additional spectrophotometry errors; see §4.2.3. **Panel C:** This panel compares the variation in the H β equivalent width rather than flux. This variation is smaller than in the H β flux, as we expect EWs to be unaffected by spectrophotometric errors.

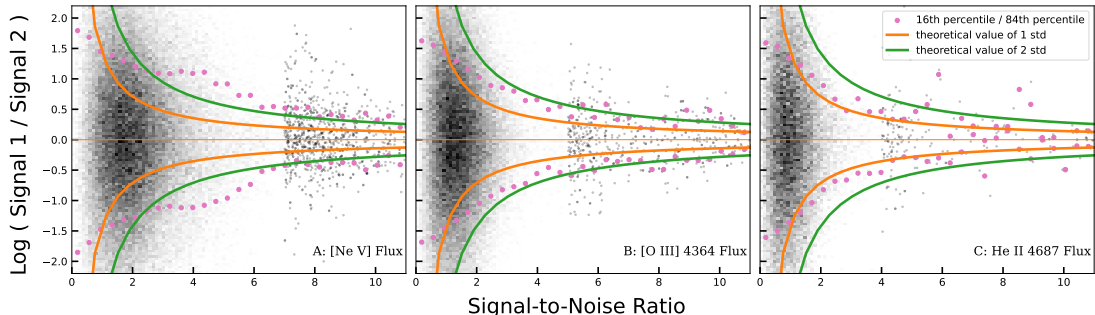


Figure 18. A comparison of line fluxes measured by the eBOSS-DAP for three weak emission lines: [Ne V] 3426, [O III] 4364, and He II 4687. These lines are only measured at $S/N > 5$ in $\sim 1\%$ of galaxies. The data is shown in grayscale and plotted as individual points above $S/N = 7, 5, 4$ in panels A, B, and C, respectively. The colored lines are the same as in Figure 17. The discrepancy between the observed (pink points) and predicted (orange line) spread of the data at $S/N = 2-6$ in [Ne V] is likely due to spurious line detections at very blue wavelengths; see §4.2.3.

collisional excitation, which [N II] is particularly sensitive to. As such, AGN will lie in the high metallicity (high N2) and high ionization (high R3) region, opposite from Star-Forming Galaxies (SFGs). Additionally, there are two other classifications: composite galaxies, which are a mix of AGN-like and SFG-like emission, and Low-Ionization Emission Line Regions (LIERs). LIERs are galaxies that see highly elevated N2 with low R3. It is unknown what mechanism drives emission in LIER galaxies; they exhibit AGN-like N2 levels, but this emission is sometimes detected far from the nuclear region, leading to debate about the cause of this radiation (F. Belfiore et al. 2016).

We first trimmed the sample down such that all BPT lines (H β , [O III] 5008, H α , and [N II] 6584) were at $S/N > 3$, and then trimmed to a redshift range of $0.0005 < z < 0.4963$. We chose this redshift cut-off to

prevent any possible systematic errors from switching the line tying from H α to H β (see §3.2.3 for details). This resulted in 94,183 spectra or $\sim 12.4\%$ of the sample in that redshift range. In Figure 21 we show the BPT diagram for this sample for redshifts below and above $z = 0.25$. As shown in Fig. 21, the different target classes lie primarily in specific parts of the BPT diagram, with ELGs and compact blue galaxies mis-targeted as quasars (QSOs) lying primarily in the star-forming region, and the other target classes having some level of AGN contribution. Of note is that, in higher redshift bins, LRG classes are more likely to host AGN.

The BPT is usable up to $z = 0.5459$, at which point H α is redshifted out of the observable window for eBOSS. Alternative AGN classification diagrams, such as MEX (S. Juneau et al. 2014) or OH-NO (L. J. Kewley et al. 2019), can be used at higher redshifts, although they

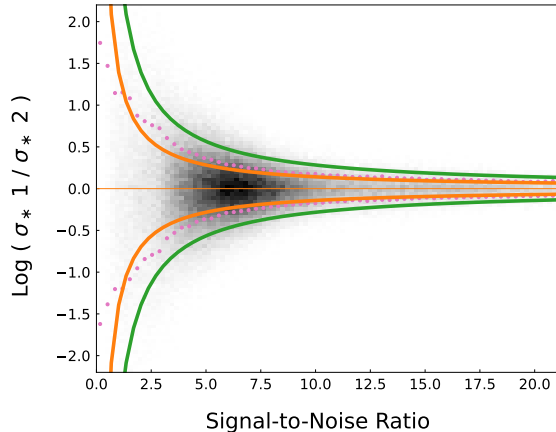


Figure 19. A comparison of the stellar velocity dispersions measured by the eBOSS-DAP in repeat spectra. The color coding is the same as in Figure 17. The good agreement between the pink dots and orange lines suggests that the velocity dispersion errors have been correctly estimated.

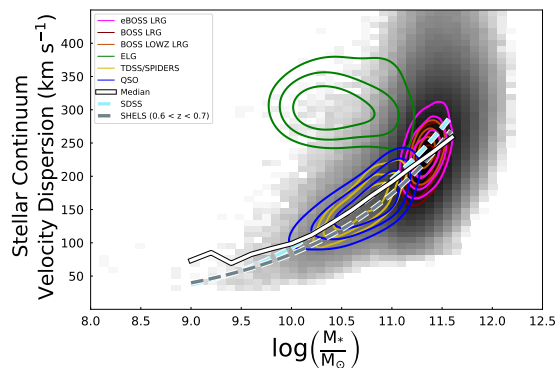


Figure 20. Stellar velocity dispersion vs. stellar mass. The grayscale is a 2D log-scaled histogram of the eBOSS galaxies with a $S/N > 5$ measurement of the stellar velocity dispersion. The contours show the different target classes; where the outermost contour for each class encloses 50% of the total sample. The median relation is shown in white. The flattened tail at low masses in this median relation may be a signature of limitations in the instrumental dispersion corrections. The dashed lines show the median relation for the SDSS-I sample (light blue) and a high- z SHELS sample (gray) found in H. J. Zahid et al. (2016). The SDSS-I sample has a redshift range $0.02 < z < 0.2$, while the SHELS sample has a higher range ($0.6 < z < 0.7$). The eBOSS sample has a redshift range of $0.0005 < z < 1.12$ with a peak at $z = 0.55$.

suffer from reduced completeness and purity (N. J. Cleri et al. 2025).

4.3.3. Star-Formation Rate vs Stellar Mass

Our third diagram is a Star-Formation Rate (SFR) versus stellar mass diagram, which is commonly used to identify star formation modes in galaxies: galaxies on the ‘main sequence’ are forming stars steadily, those above it are in a starburst phase, while those below may be quenching or already passive. Additionally, the star-forming main sequence evolves over redshift, moving towards higher average star-formation rates for galaxies at higher redshifts (c.f. P. Popesso et al. 2023). To make this diagram, we require $[\text{O III}]$ 5008 and $[\text{N II}]$ 6584 $S/N > 3$ and $\text{H}\beta$ and $\text{H}\alpha$ $S/N > 5$. The Balmer lines have a higher S/N cut as they are used to compute the

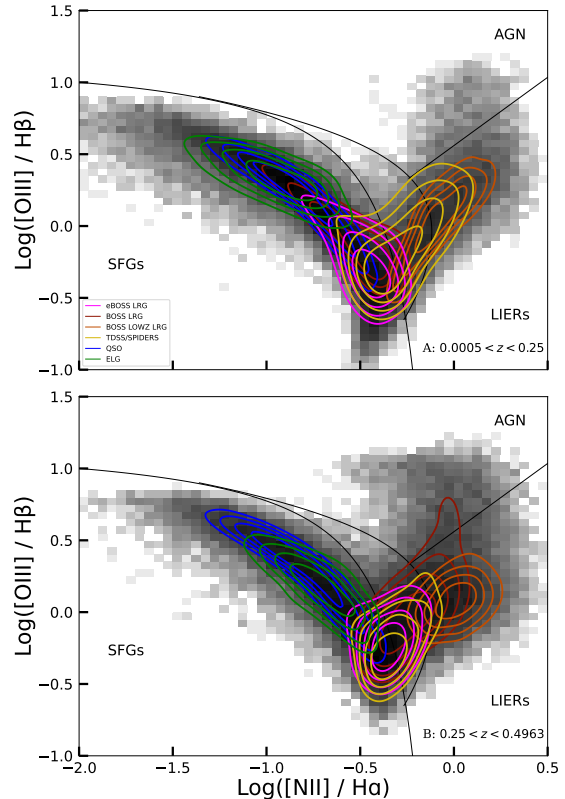


Figure 21. BPT diagram in two redshift ranges ($0.0005 < z < 0.25$ and $0.25 < z < 0.4963$). The eBOSS data are shown as 2D log-scaled histograms. Contours show the location of different target classes; they begin at 50% of the data. The diagram is divided into regions representing different ionization sources following D. R. Law et al. (2021c). ‘AGN’ are Active Galactic Nuclei, ‘SFGs’ are Star-Forming Galaxies, ‘LIERs’ are Low Ionization Emission Regions, and finally, the unlabeled region between SFGs and AGN is composite galaxies.

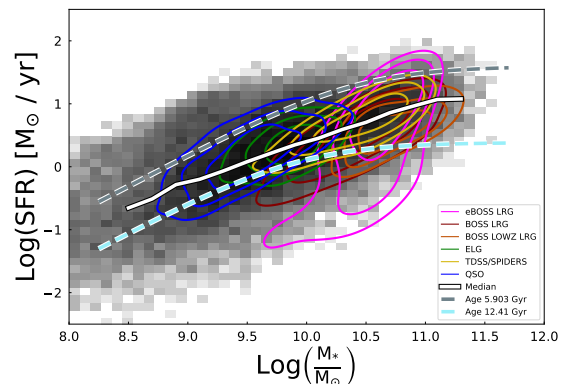


Figure 22. The Star-Formation Rate (SFR; found through $\text{H}\alpha$ luminosity) vs stellar mass (M_* ; found with CIGALE) diagram for star-forming galaxies at $0.0005 < z < 0.4963$. The eBOSS data for BPT-selected star-forming galaxies with $S/N > 3$ $[\text{O III}]$ 5008 and $[\text{N II}]$ 6584 lines and $S/N > 5$ $\text{H}\beta$ and $\text{H}\alpha$ lines is shown as a 2D log-scaled histogram (grayscale). Colored contours show the location of different target classes; contours begin at 50% of the data. The median line has been plotted in white; orange and blue lines show the star-forming main sequence from P. Popesso et al. (2023) at ages of 12.41 Gyr ($z = 0.1$) and 5.903 Gyr ($z = 1$), respectively.

extinction correction of the spectra before determining the star formation rate. We then trim the sample to in-

clude only galaxies that were classified as a BPT SFG using the D. R. Law et al. (2021c) lines. This resulted in 44,406 galaxies or $\sim 6\%$ of the sample in this redshift range ($0.0005 < z < 0.4963$), or $\sim 47\%$ of galaxies that pass the BPT cuts.

We compute the extinction corrected $H\alpha$ luminosity by first computing $E(B - V)$ from $\frac{H\alpha}{H\beta}$. We then use the same `dust_extinction` package to find the correction and apply it to the $H\alpha$ luminosity. We then calculate star formation rates for this subsample using the extinction corrected $H\alpha$ luminosity and the R. C. Kennicutt & N. J. Evans (2012) calibration. We plot the 2D log-scaled histogram of the SFRs versus the masses of the subsample, as well as the star-forming main sequence from P. Popesso et al. (2023) for ages of 5.903 Gyr ($z = 1$) and 12.41 Gyr ($z = 0.1$) in Figure 22.

Our median lies comfortably between the two star-forming main sequences, chosen by finding the ages of the universe at the maximum and minimum redshifts of our sample. Additionally, we find that galaxies targeted as ELGs and QSOs have characteristically lower masses than the LRG targets, and they are more likely to be on the main sequence.

Of note is that we only show BPT SFGs in this figure. This is because we use $H\alpha$ as our star formation rate indicator, and it is not a reliable indicator for BPT LIERs and AGN. These two populations typically fall below the main sequence (c.f., D. Miller et al., in prep.).

4.3.4. Mass–Metallicity Relation

Our penultimate sample characterization is the stellar mass – gas-phase metallicity relation (MZR). The MZR is extremely tight (± 0.1 dex) at $z \sim 0.1$ (C. A. Tremonti et al. 2004), and it has been shown to evolve mildly with redshift (H. J. Zahid et al. 2014; Z. J. Lewis et al. 2023). Galaxies classified as AGN according to the D. R. Law et al. (2021c) BPT diagram are removed from the sample, as are galaxies with [O II] 3727, 3729, $H\beta$, [O III] 5008, $H\alpha$, and [N II] 6584 lines with $S/N < 3$. These cuts yield 46,098 spectra, corresponding to roughly 73% of the 63,182 BPT SFGs. Metallicities are calculated according to the $\log\left(\frac{[\text{O II}] 3727, 3729 + [\text{O III}] 5008}{H\beta}\right)$ (R23) diagnostic calibration of K. Nakajima et al. (2022), and the double-branching is broken using the excitation parameter $\log\left(\frac{[\text{O III}] 5008}{[\text{O II}] 3727, 3729}\right)$ (O32).

We plot our findings in Fig. 23. Panel A shows the MZR for our sample in the redshift range $0.0005 < z < 0.4963$ along with target classification contours. Here we see that LRGs have both higher masses and higher metallicities than ELGs and QSO targets. We grouped LRGs and TDSS/SPIDERS spectra, as well as ELGs and QSOs, to find mass–metallicity relations for both broad classes of objects. These relations are observed to exhibit the expected correlation, including both the power-law rise at low stellar masses in ELGs and the metallicity saturation and plateau at higher stellar masses in LRGs with an average $\sigma_{\text{ELG}} \simeq 0.101$ dex and $\sigma_{\text{LRG}} \simeq 0.108$

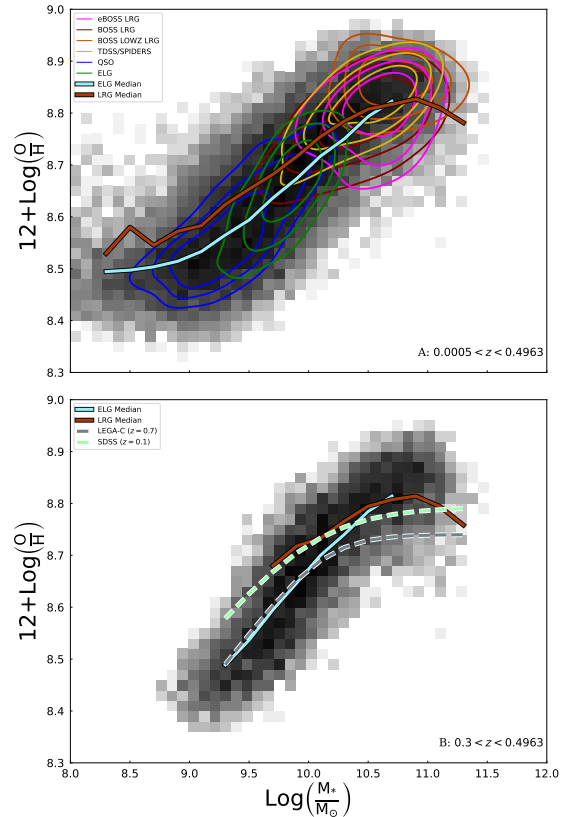


Figure 23. The mass–metallicity relation for eBOSS galaxies. This figure follows the plotting scheme of Fig. 22. Metallicities are determined using the empirical calibrations of K. Nakajima et al. (2022), which employ the R23 calibration and the O32 parameter to break the double-branching. **Panel A:** The data in the redshift range $0.0005 < z < 0.4963$ is shown in grayscale, with contours representing different target classes. **Panel B:** The data is trimmed to the redshift range $0.3 < z < 0.4963$ to limit the redshift evolution and remove cases of H II regions classified as galaxies (see §2.5). In both panels, the rust-red solid lines denote the medians for LRG and TDSS/SPIDERS spectra, whereas the light-blue solid lines denote the medians for ELG and QSO spectra, these lines ignore the outer 1% of the sample. For comparison, we plot the MZR found in LEGA-C for $z \sim 0.7$ by Z. J. Lewis et al. (2024) in a gray dashed line and the SDSS-I MZR at $z \simeq 0.1$ found by M. Curti et al. (2020) in a green dashed line. The differences in trends between LRGs and ELGs highlight the importance of sample selection.

dex. ELGs show lower metallicity at a given mass than LRGs for all but the highest masses. At $10^{9.5} M_{\odot}$, the metallicity difference is 0.06 dex, highlighting the importance of sample selection.

For Panel B we trimmed the sample further to the redshift range $0.3 < z < 0.4963$ resulting in 13,866 spectra. This was done to avoid cases of H II regions classified as galaxies (see §2.5), which cause the metal-rich but low-mass outliers seen in Panel A. (These galaxies have artificially low stellar masses due to deblending problems in the SDSS photometry.) Another benefit of the trim was the ability to restrict the redshift evolution of the MZR, which is a major source of the scatter in Panel A. As seen in Panel B, the correlation of the MZRs is tighter in this redshift range with an average $\sigma_{\text{ELG}} \simeq 0.09$ dex and $\sigma_{\text{LRG}} \simeq 0.101$ dex.

For comparison, in Figure 23 panel B we plot the me-

dian MZR of the SDSS-I sample ($z \simeq 0.1$) found by M. Curti et al. (2020) and the median MZR of the LEGA-C survey ($z = 0.7$) found by Z. J. Lewis et al. (2024). The LEGA-C sample is K-band selected and relatively mass-complete (A. van der Wel et al. 2016). Both samples use very similar metallicity measurements to ours, mitigating strong line abundance calibration systematics. Given the redshift of the eBOSS sample used in this comparison ($z \sim 0.4$), we expect the median MZR of the ELGs and LRGs to lie between those of the SDSS-I ($z \sim 0.1$) and LEGA-C ($z \sim 0.7$) samples. However, this is not what we find. The LRGs show a fairly good match to the SDSS-I MZR over most of the mass range with a slightly elevated metallicity at $\log(M_*) = 10.5 - 11$. The LRGs were selected for their large 4000-Å breaks and red colors, a selection which favors older and dustier star-forming galaxies. Both stellar population age and dust attenuation may have residual correlations with metallicity, accounting for the fact that $z \sim 0.4$ eBOSS LRGs have an MZR more similar to $z \sim 0.1$ galaxies. In contrast, the eBOSS ELG MZR matches that of the $z \sim 0.7$ LEGA-C sample until about $10^{10} M_\odot$ after which the median metallicity becomes higher than that of LEGA-C and even exceeds the median metallicity of SDSS-I galaxies in the most massive bin. The ELGs were selected based on their blue colors, which may be linked with less dust/metals, and higher rates of star formation due to recent gas inflows, causing them to better match the MZR of high redshift galaxies. The higher metallicities seen above $\log(M_*)$ are more difficult to explain, and may have to do with survey volume differences between LEGA-C and eBOSS. In any case, the impact of sample selection effects on the MZR is evident. A more thorough analysis of these differences will be the subject of future work.

4.3.5. $H\delta_A$ vs $Dn4000$

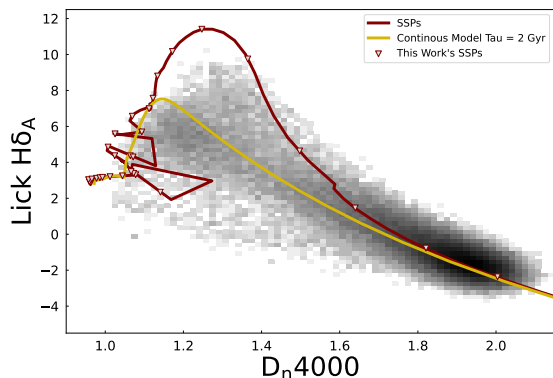


Figure 24. A spectral index diagram of $H\delta_A$ vs $Dn4000$. Spectra that pass the $H\delta_A$ error < 0.8 and $Dn4000$ error < 0.03 cuts from G. Kauffmann et al. (2003) (approximately 3.3% of the sample) are shown as a 2D log-scaled histogram (grayscale). Overplotted is an evolutionary sequence for a continuous star formation sequence (yellow) as well as a simple stellar population (dark red). The red triangles denote the exact values of the solar-metallicity SSPs used in this work.

Our final example is the $H\delta_A$ versus $Dn4000$ spectral indices plot (Fig. 24). To start, we applied the cuts found in G. Kauffmann et al. (2003) of $H\delta_A$ error < 0.8 and $Dn4000$ error < 0.03 . We then removed spectra with unphysical index values and limited the redshift to $0.05 < z < 0.8$, resulting in 65,184 spectra or merely $\sim 3.4\%$ of our full sample. The majority of eBOSS galaxies have stellar continua that are too low S/N for the line indices to be measured accurately.

By comparing the $Dn4000$ and $H\delta_A$ indices, we gain insight into the average stellar populations of this relatively bright sub-sample of eBOSS galaxies. $Dn4000$ traces the 4000-Å break and indicates the mean age of the stellar population; a low $Dn4000$ value suggests a young stellar population, while a high $Dn4000$ value indicates older stars. The $H\delta_A$ index traces the strength of stellar Balmer absorption, which peaks at ages of a few 100 Myr, when A-stars dominate the spectrum.

In Figure 24, we overplot the $Dn4000$ and $H\delta_A$ values of two stellar population models: Solar metallicity SSPs and a continuous star formation model in red and yellow, respectively. A continuous star formation history model is a good match to the bulk of our data, but some galaxies with extreme Balmer absorption lie closer to the SSP models; such galaxies are likely post-starburst galaxies (K. D. French 2021). Many of the galaxies that lie well below the continuous models appear to be blazars: early-type galaxies with an additional power law continuum contribution arising from a relativistically beamed jet.

5. SUMMARY

This work presents the initial release and analysis of data and software products from the eBOSS Data Analysis Pipeline (eBOSS-DAP), designed to extend the utility of spectral data from the Extended Baryon Oscillation Spectroscopic Survey (eBOSS; K. S. Dawson et al. 2016b). Previously, these data had primarily been utilized for measuring cosmological parameters. By using the eBOSS-DAP, we were able to extend the functionality of the survey and robustly characterize the eBOSS sample. Our main findings are as follows:

1. We characterized the eBOSS galaxy sample which includes galaxies targeted using a variety of color-based target selection algorithms (See §2). There are 1,901,834 spectra with 197,521 duplicates (1,704,313 unique galaxies) with a range of $z = 0$ to $z = 1.12$ (Fig. 1) and an average of 52% of their light down the fiber (Fig. 4). These spectra have an average S/N that peaks at $S/N = 1.88$ with an extended tail towards higher values (Fig. 2). We grouped the galaxies into 6 classes based on their target selection. The properties of these target classes are elucidated in Figures 3 and 20 – 23.
2. We made extensive use of the duplicate spectra to characterize the eBOSS survey’s spectrophotometric calibration (§2.4). We show that spectrophotometry errors are strongly wavelength-dependent.

For most eBOSS galaxies, relative flux calibration error is less than 10% between 4488 – 8397 Å with errors exceeding 50% at wavelengths less than 3665 Å or greater than 10283 Å (Fig.6)

3. We provide a pipeline overview in which we detail how the MaNGA-DAP was modified to become the eBOSS-DAP (§3). The eBOSS-DAP utilizes algorithms from the MaNGA-DAP to process one-dimensional galaxy spectra from the eBOSS dataset, extracting comprehensive emission line fluxes, kinematics, continuum spectral indices, and spectral template weights. Like the MaNGA-DAP, the eBOSS-DAP can be easily adapted to work on datasets beyond eBOSS. Some key features of the eBOSS-DAP include: flexibility in adjusting emission line lists, spectral indices, and stellar templates, and tools for modifying fits, such as tying emission line parameters for improved precision.
4. Our final data products include emission line flux measurements (Fig. 13), spectral index measurements (Fig. 14), kinematics, and best-fit continuum models. We create three catalogs: a full sample (1,899,553 spectra) emission line catalog with a reduced emission line list (27 lines), a high equivalent width sample (167,466 spectra) emission line catalog which makes use of the full line list (78 lines), and a catalog of the spectral indices and the weights of the stellar continuum templates. In addition, we store the stellar continuum and emission-line fits for each spectrum as FITS files. All of these data products, as well as a suite of tools including the eBOSS-DAP source code, will be available for public access (see Data Availability for details).
5. We provide catalog validation metrics, such as comparisons of emission-line fluxes in repeat spectra (Figures 17 and 18) and comparisons with fluxes measured by the SDSS pipeline (A. S. Bolton et al. 2012) (Fig. 16). Generally, we find the expected level of agreement between the fluxes given the errors, except at high S/N, where the spectrophotometric error becomes dominant. We provide average correction terms for a few commonly used lines and line ratios to approximately account for the spectrophotometric error (Table 1).
6. We use the eBOSS-DAP data to construct various galaxy scaling relations (Figures 20 - 24), highlighting the 6 target classes. We caution users of the data to account for sample selection effects when pursuing scientific applications.

In summary, we have produced an extensive set of well-characterized emission line measurements for the 1.7 million galaxies in the eBOSS sample. This data will be useful for a variety of statistical studies of galaxy evolution at $z < 1$. The eBOSS-DAP catalogs will be of particular value for AGN studies due to the sample makeup and the

expanded line list with Matthews Acuña et al, in prep, focusing on utilizing the high quantity of [Ne V] 3347, 3427 detections to study coronal line detections in AGN.

ACKNOWLEDGMENTS

OMA, CAT, and DM gratefully acknowledge support for this work from NSF grant AST-2107725. OMA thanks I. McConachie, I. Laseter, and M. Maseda for helpful comments. AD-S gratefully acknowledges support for this work from NSF grant 2107726. BL gratefully acknowledges support for this work from NSF grant 2107727. ZJL acknowledges support from the National Science Foundation Graduate Research Fellowship under grant No. 2137424.

This research uses services or data provided by the Astro Data Lab at NSF’s NOIRLab. NOIRLab is operated by the Association of Universities for Research in Astronomy (AURA), Inc. under a cooperative agreement with the National Science Foundation.

Funding for the Sloan Digital Sky Survey IV has been provided by the Alfred P. Sloan Foundation, the U.S. Department of Energy Office of Science, and the Participating Institutions. SDSS-IV acknowledges support and resources from the Center for High-Performance Computing at the University of Utah. The SDSS website is available at www.sdss.org. SDSS-IV is managed by the Astrophysical Research Consortium for the Participating Institutions of the SDSS Collaboration including the Brazilian Participation Group, the Carnegie Institution for Science, Carnegie Mellon University, the Chilean Participation Group, the French Participation Group, Harvard-Smithsonian Center for Astrophysics, Instituto de Astrofísica de Canarias, The Johns Hopkins University, Kavli Institute for the Physics and Mathematics of the Universe (IPMU)/University of Tokyo, Lawrence Berkeley National Laboratory, Leibniz Institut für Astrophysik Potsdam (AIP), Max-Planck-Institut für Astronomie (MPIA Heidelberg), MaxPlanck-Institut für Astrophysik (MPA Garching), Max-Planck-Institut für Extraterrestrische Physik (MPE), National Astronomical Observatories of China, New Mexico State University, New York University, University of Notre Dame, Observatório Nacional/MCTI, The Ohio State University, Pennsylvania State University, Shanghai Astronomical Observatory, United Kingdom Participation Group, Universidad Nacional Autónoma de México, University of Arizona, University of Colorado Boulder, University of Oxford, University of Portsmouth, University of Utah, University of Virginia, University of Washington, University of Wisconsin, Vanderbilt University, and Yale University.

SOFTWARE

This research made use of *Astropy*, a community-developed core Python package for Astronomy (Astropy Collaboration et al. 2013, 2018, 2022); *dust-extinction* (K. D. Gordon 2024); *dustmaps* (G. Green 2018); *FSPS* (C. Conroy et al. 2009; C. Conroy & J. E. Gunn

2010) and its Python bindings package `Python-FSPS`¹¹; `IPython` (F. Pérez & B. E. Granger 2007); `MaNGA-DAP` (K. B. Westfall et al. 2019; F. Belfiore et al. 2019); `matplotlib` (J. D. Hunter 2007); `numpy` (C. R. Harris et al. 2020); `scipy` (Jones et al. 2001); `pandas` (The pandas development team 2020; Wes McKinney 2010); `SciPy` (P. Virtanen et al. 2020); and `Seaborn` (M. L. Waskom 2021)

Additionally, computing resources from the Center for High Throughput Computing (Center for High Throughput Computing 2006) were used to run the pipeline.

DATA AVAILABILITY

All catalogs in this paper are available at <https://datalab.noirlab.edu/data/sdss#sdss-iv-eboss-dap-value-added-catalog>.

The eBOSS-DAP is available at <https://github.com/owenmatthewsa/ebossdap>. The data used in the plots within this article are available on request to the author.

REFERENCES

- Abazajian, K., Adelman-McCarthy, J. K., Agüeros, M. A., et al. 2004 *AJ*, 128, 502, doi: 10.1086/421365
- Abazajian, K. N., Adelman-McCarthy, J. K., Agüeros, M. A., et al. 2009 *ApJS*, 182, 543, doi: 10.1088/0067-0049/182/2/543
- Abdurro'uf, Accetta, K., Aerts, C., et al. 2022a *ApJS*, 259, 35, doi: 10.3847/1538-4365/ac4414
- Abdurro'uf, Accetta, K., Aerts, C., et al. 2022b *ApJS*, 259, 35, doi: 10.3847/1538-4365/ac4414
- Anand, A., Nelson, D., & Kauffmann, G. 2021 *MNRAS*, 504, 65, doi: 10.1093/mnras/stab871
- Andrews, B. H., & Martini, P. 2013 *ApJ*, 765, 140, doi: 10.1088/0004-637X/765/2/140
- Asa'd, R., Coelho, P. R. T., John, J. M., et al. 2025 *AJ*, 170, 85, doi: 10.3847/1538-3881/adaaad
- Astropy Collaboration, Robitaille, T. P., Tollerud, E. J., et al. 2013 *A&A*, 558, A33, doi: 10.1051/0004-6361/201322068
- Astropy Collaboration, Price-Whelan, A. M., Sipőcz, B. M., et al. 2018 *AJ*, 156, 123, doi: 10.3847/1538-3881/aabc4f
- Astropy Collaboration, Price-Whelan, A. M., Lim, P. L., et al. 2022 *ApJ*, 935, 167, doi: 10.3847/1538-4357/ac7c74
- Baldwin, J. A., Phillips, M. M., & Terlevich, R. 1981 *PASP*, 93, 5, doi: 10.1086/130766
- Belfiore, F., Maiolino, R., Maraston, C., et al. 2016 *MNRAS*, 461, 3111, doi: 10.1093/mnras/stw1234
- Belfiore, F., Westfall, K. B., Schaefer, A., et al. 2019 *AJ*, 158, 160, doi: 10.3847/1538-3881/ab3e4e
- Blanton, M. R., & Moustakas, J. 2009 *ARA&A*, 47, 159, doi: 10.1146/annurev-astro-082708-101734
- Blanton, M. R., Bershady, M. A., Abolfathi, B., et al. 2017 *AJ*, 154, 28, doi: 10.3847/1538-3881/aa7567
- Bolton, A. S., Schlegel, D. J., Aubourg, É., et al. 2012 *AJ*, 144, 144, doi: 10.1088/0004-6256/144/5/144
- Boquien, M., Burgarella, D., Roehly, Y., et al. 2019 *A&A*, 622, A103, doi: 10.1051/0004-6361/201834156
- Brinchmann, J., Charlot, S., Heckman, T. M., et al. 2004, Stellar masses, star formation rates, metallicities and AGN properties for 200,000 galaxies in the SDSS Data Release Two (DR2), <https://arxiv.org/abs/astro-ph/0406220>
- Bruzual, G., & Charlot, S. 2003 *MNRAS*, 344, 1000, doi: 10.1046/j.1365-8711.2003.06897.x
- Bundy, K., Bershady, M. A., Law, D. R., et al. 2015 *ApJ*, 798, 7, doi: 10.1088/0004-637X/798/1/7
- Byler, N., Dalcanton, J. J., Conroy, C., & Johnson, B. D. 2017 *ApJ*, 840, 44, doi: 10.3847/1538-4357/aa6c66
- Byrne, C. M., & Stanway, E. R. 2023 *MNRAS*, 521, 4995, doi: 10.1093/mnras/stad832
- Calzetti, D., Armus, L., Bohlin, R. C., et al. 2000 *ApJ*, 533, 682, doi: 10.1086/308692
- Cappellari, M. 2012, pPXF: Penalized Pixel-Fitting stellar kinematics extraction, Astrophysics Source Code Library, record ascl:1210.002
- Cappellari, M. 2023 *MNRAS*, 526, 3273, doi: 10.1093/mnras/stad2597
- Castelli, F. 2005 *Memorie della Societa Astronomica Italiana Supplementi*, 8, 25
- Center for High Throughput Computing. 2006, Center for High Throughput Computing, Center for High Throughput Computing, doi: 10.21231/GNT1-HW21
- Chabrier, G. 2003 *PASP*, 115, 763, doi: 10.1086/376392
- Chattopadhyay, S., Bershady, M. A., Law, D. R., et al. 2024 *MNRAS*, 528, 5377, doi: 10.1093/mnras/stae371
- Chiang, Y.-K. 2023 *ApJ*, 958, 118, doi: 10.3847/1538-4357/acf4a1
- Choi, J., Dotter, A., Conroy, C., et al. 2016 *ApJ*, 823, 102, doi: 10.3847/0004-637X/823/2/102
- Clerc, N., Merloni, A., Zhang, Y. Y., et al. 2016 *MNRAS*, 463, 4490, doi: 10.1093/mnras/stw2214
- Cleri, N. J., Olivier, G. M., Backhaus, B. E., et al. 2025 *arXiv e-prints*, arXiv:2506.21660, doi: 10.48550/arXiv.2506.21660
- Coelho, P. R. T., Bruzual, G., & Charlot, S. 2020 *MNRAS*, 491, 2025, doi: 10.1093/mnras/stz3023
- Conroy, C. 2013 *ARA&A*, 51, 393, doi: 10.1146/annurev-astro-082812-141017
- Conroy, C., & Gunn, J. E. 2010 *ApJ*, 712, 833, doi: 10.1088/0004-637X/712/2/833
- Conroy, C., Gunn, J. E., & White, M. 2009 *ApJ*, 699, 486, doi: 10.1088/0004-637X/699/1/486
- Curti, M., Mannucci, F., Cresci, G., & Maiolino, R. 2020 *MNRAS*, 491, 944, doi: 10.1093/mnras/stz2910
- Dawson, K. S., Schlegel, D. J., Ahn, C. P., et al. 2013 *AJ*, 145, 10, doi: 10.1088/0004-6256/145/1/10
- Dawson, K. S., Kneib, J.-P., Percival, W. J., et al. 2016a *AJ*, 151, 44, doi: 10.3847/0004-6256/151/2/44
- Dawson, K. S., Kneib, J.-P., Percival, W. J., et al. 2016b *AJ*, 151, 44, doi: 10.3847/0004-6256/151/2/44
- Dey, A., Schlegel, D. J., Lang, D., et al. 2019 *AJ*, 157, 168, doi: 10.3847/1538-3881/ab089d
- Dotter, A. 2016 *ApJS*, 222, 8, doi: 10.3847/0067-0049/222/1/8
- Draine, B. T., Aniano, G., Krause, O., et al. 2014 *ApJ*, 780, 172, doi: 10.1088/0004-637X/780/2/172
- Dwelly, T., Salvato, M., Merloni, A., et al. 2017 *MNRAS*, 469, 1065, doi: 10.1093/mnras/stx864
- Eisenstein, D. J., Annis, J., Gunn, J. E., et al. 2001 *AJ*, 122, 2267, doi: 10.1086/323717
- Eisenstein, D. J., Zehavi, I., Hogg, D. W., et al. 2005 *ApJ*, 633, 560, doi: 10.1086/466512
- Eisenstein, D. J., Weinberg, D. H., Agol, E., et al. 2011 *AJ*, 142, 72, doi: 10.1088/0004-6256/142/3/72
- Filippenko, A. V. 1982a *PASP*, 94, 715, doi: 10.1086/131052
- Filippenko, A. V. 1982b *PASP*, 94, 715, doi: 10.1086/131052
- Fitzpatrick, M. J., Olsen, K., Economou, F., et al. 2014, in *Society of Photo-Optical Instrumentation Engineers (SPIE) Conference Series*, Vol. 9149, *Observatory Operations: Strategies, Processes, and Systems V*, ed. A. B. Peck, C. R. Benn, & R. L. Seaman, 91491T, doi: 10.1117/12.2057445
- French, K. D. 2021 *PASP*, 133, 072001, doi: 10.1088/1538-3873/ac0a59
- Fukugita, M., Ichikawa, T., Gunn, J. E., et al. 1996 *AJ*, 111, 1748, doi: 10.1086/117915
- Geller, M. J., Dell'Antonio, I. P., Kurtz, M. J., et al. 2005 *ApJL*, 635, L125, doi: 10.1086/499399
- Geller, M. J., Hwang, H. S., Dell'Antonio, I. P., et al. 2016 *ApJS*, 224, 11, doi: 10.3847/0067-0049/224/1/11
- Geller, M. J., Hwang, H. S., Fabricant, D. G., et al. 2014 *ApJS*, 213, 35, doi: 10.1088/0067-0049/213/2/35
- Gordon, K. D. 2024 *Journal of Open Source Software*, 9, 7023, doi: 10.21105/joss.07023
- Gordon, K. D., Cartledge, S., & Clayton, G. C. 2009 *ApJ*, 705, 1320, doi: 10.1088/0004-637X/705/2/1320
- Green, G. 2018 *The Journal of Open Source Software*, 3, 695, doi: 10.21105/joss.00695
- Gunn, J. E., Carr, M., Rockosi, C., et al. 1998 *AJ*, 116, 3040, doi: 10.1086/300645

¹¹ <https://github.com/dfm/python-fsps>

- Gunn, J. E., Siegmund, W. A., Mannery, E. J., et al. 2006 *AJ*, 131, 2332, doi: 10.1086/500975
- Harris, C. R., Millman, K. J., van der Walt, S. J., et al. 2020 *Nature*, 585, 357, doi: 10.1038/s41586-020-2649-2
- Heckman, T. M., Kauffmann, G., Brinchmann, J., et al. 2004 *ApJ*, 613, 109, doi: 10.1086/422872
- Hunter, J. D. 2007 *Computing in Science & Engineering*, 9, 90, doi: 10.1109/MCSE.2007.55
- Ji, X., & Yan, R. 2022 *A&A*, 659, A112, doi: 10.1051/0004-6361/202142312
- Juneau, S., Bournaud, F., Charlot, S., et al. 2014 *ApJ*, 788, 88, doi: 10.1088/0004-637X/788/1/88
- Kauffmann, G., White, S. D. M., Heckman, T. M., et al. 2004 *MNRAS*, 353, 713, doi: 10.1111/j.1365-2966.2004.08117.x
- Kauffmann, G., White, S. D. M., Heckman, T. M., et al. 2004 *Monthly Notices of the Royal Astronomical Society*, 353, 713, doi: 10.1111/j.1365-2966.2004.08117.x
- Kauffmann, G., Heckman, T. M., White, S. D. M., et al. 2003 *MNRAS*, 341, 33, doi: 10.1046/j.1365-8711.2003.06291.x
- Kennicutt, R. C., & Evans, N. J. 2012 *ARA&A*, 50, 531, doi: 10.1146/annurev-astro-081811-125610
- Kewley, L. J., Dopita, M. A., Leitherer, C., et al. 2013 *ApJ*, 774, 100, doi: 10.1088/0004-637X/774/2/100
- Kewley, L. J., & Ellison, S. L. 2008 *ApJ*, 681, 1183, doi: 10.1086/587500
- Kewley, L. J., Groves, B., Kauffmann, G., & Heckman, T. 2006 *MNRAS*, 372, 961, doi: 10.1111/j.1365-2966.2006.10859.x
- Kewley, L. J., Nicholls, D. C., & Sutherland, R. S. 2019 *ARA&A*, 57, 511, doi: 10.1146/annurev-astro-081817-051832
- Kurucz, R. L. 1970 *SAO Special Report*, 309
- Kurucz, R. L. 1993, *SYNTHE spectrum synthesis programs and line data*
- Lan, T.-W., & Mo, H. 2018 *ApJ*, 866, 36, doi: 10.3847/1538-4357/aadc08
- Law, D. R., Westfall, K. B., Bershady, M. A., et al. 2021a *AJ*, 161, 52, doi: 10.3847/1538-3881/abcaa2
- Law, D. R., Westfall, K. B., Bershady, M. A., et al. 2021b *AJ*, 161, 52, doi: 10.3847/1538-3881/abcaa2
- Law, D. R., Ji, X., Belfiore, F., et al. 2021c *ApJ*, 915, 35, doi: 10.3847/1538-4357/abfe0a
- Lewis, Z. J., Andrews, B. H., Bezanson, R., et al. 2023, *The Gas-Phase Mass–Metallicity Relation for Massive Galaxies at $z \sim 0.7$ with the LEGA-C Survey*, <https://arxiv.org/abs/2304.12343>
- Lewis, Z. J., Andrews, B. H., Bezanson, R., et al. 2024 *ApJ*, 964, 59, doi: 10.3847/1538-4357/ad250c
- Lupton, R., Gunn, J. E., Ivezić, Z., Knapp, G. R., & Kent, S. 2001, in *Astronomical Society of the Pacific Conference Series*, Vol. 238, *Astronomical Data Analysis Software and Systems X*, ed. J. Harnden, F. R., F. A. Primini, & H. E. Payne, 269, doi: 10.48550/arXiv.astro-ph/0101420
- Mannucci, F., Cresci, G., Maiolino, R., Marconi, A., & Gnerucci, A. 2010 *MNRAS*, 408, 2115, doi: 10.1111/j.1365-2966.2010.17291.x
- Maraston, C., & Strömbäck, G. 2011 *MNRAS*, 418, 2785, doi: 10.1111/j.1365-2966.2011.19738.x
- Morganson, E., Green, P. J., Anderson, S. F., et al. 2015 *ApJ*, 806, 244, doi: 10.1088/0004-637X/806/2/244
- Myers, A. D., Palanque-Delabrouille, N., Prakash, A., et al. 2015 *The Astrophysical Journal Supplement Series*, 221, 27, doi: 10.1088/0067-0049/221/2/27
- Nakajima, K., Ouchi, M., Xu, Y., et al. 2022 *ApJS*, 262, 3, doi: 10.3847/1538-4365/ac7710
- Nikutta, R., Fitzpatrick, M., Scott, A., & Weaver, B. 2020 *Astronomy and Computing*, 33, 100411, doi: <https://doi.org/10.1016/j.ascom.2020.100411>
- O'Donnell, J. E. 1994 *ApJ*, 422, 158, doi: 10.1086/173713
- Oke, J. B. 1990 *AJ*, 99, 1621, doi: 10.1086/115444
- Peng, Y.-j., Lilly, S. J., Kovač, K., et al. 2010 *ApJ*, 721, 193, doi: 10.1088/0004-637X/721/1/193
- Pérez, F., & Granger, B. E. 2007 *Computing in Science and Engineering*, 9, 21, doi: 10.1109/MCSE.2007.53
- Popesso, P., Concas, A., Cresci, G., et al. 2023 *MNRAS*, 519, 1526, doi: 10.1093/mnras/stac3214
- Prakash, A., Licquia, T. C., Newman, J. A., et al. 2016 *The Astrophysical Journal Supplement Series*, 224, 34, doi: 10.3847/0067-0049/224/2/34
- Prugniel, P., & Soubiran, C. 2001 *A&A*, 369, 1048, doi: 10.1051/0004-6361:20010163
- Raichoor, A., Comparat, J., Delubac, T., et al. 2017 *MNRAS*, 471, 3955, doi: 10.1093/mnras/stx1790
- Raichoor, A., de Mattia, A., Ross, A. J., et al. 2021 *MNRAS*, 500, 3254, doi: 10.1093/mnras/staa3336
- Reid, B., Ho, S., Padmanabhan, N., et al. 2016 *MNRAS*, 455, 1553, doi: 10.1093/mnras/stv2382
- Salim, S., Lee, J. C., Ly, C., et al. 2014 *ApJ*, 797, 126, doi: 10.1088/0004-637X/797/2/126
- Smee, S. A., Gunn, J. E., Uomoto, A., et al. 2013 *AJ*, 146, 32, doi: 10.1088/0004-6256/146/2/32
- Stoughton, C., Lupton, R. H., Bernardi, M., et al. 2002 *AJ*, 123, 485, doi: 10.1086/324741
- Strauss, M. A., Weinberg, D. H., Lupton, R. H., et al. 2002 *AJ*, 124, 1810, doi: 10.1086/342343
- The pandas development team. 2020, *pandas-dev/pandas: Pandas*, latest Zenodo, doi: 10.5281/zenodo.3509134
- Tremonti, C. A., Heckman, T. M., Kauffmann, G., et al. 2004 *ApJ*, 613, 898, doi: 10.1086/423264
- van der Wel, A., Noeske, K., Bezanson, R., et al. 2016 *ApJS*, 223, 29, doi: 10.3847/0067-0049/223/2/29
- Virtanen, P., Gommers, R., Oliphant, T. E., et al. 2020 *Nature Methods*, 17, 261, doi: 10.1038/s41592-019-0686-2
- Wang, B., Leja, J., de Graaff, A., et al. 2024 *ApJL*, 969, L13, doi: 10.3847/2041-8213/ad55f7
- Waskom, M. L. 2021 *Journal of Open Source Software*, 6, 3021, doi: 10.21105/joss.03021
- Weinmann, S. M., van den Bosch, F. C., Yang, X., & Mo, H. J. 2006 *MNRAS*, 366, 2, doi: 10.1111/j.1365-2966.2005.09865.x
- Wes McKinney. 2010, in *Proceedings of the 9th Python in Science Conference*, ed. Stéfan van der Walt & Jarrod Millman, 56 – 61, doi: 10.25080/Majora-92bf1922-00a
- Westfall, K. B., Cappellari, M., Bershady, M. A., et al. 2019 *AJ*, 158, 231, doi: 10.3847/1538-3881/ab44a2
- Wright, E. L., Eisenhardt, P. R. M., Mainzer, A. K., et al. 2010 *AJ*, 140, 1868, doi: 10.1088/0004-6256/140/6/1868
- York, D. G., Adelman, J., Anderson, John E., J., et al. 2000 *AJ*, 120, 1579, doi: 10.1086/301513
- Zahid, H. J., Dima, G. I., Kudritzki, R.-P., et al. 2014 *ApJ*, 791, 130, doi: 10.1088/0004-637X/791/2/130
- Zahid, H. J., Geller, M. J., Fabricant, D. G., & Hwang, H. S. 2016 *ApJ*, 832, 203, doi: 10.3847/0004-637X/832/2/203
- Zhu, G. B., Comparat, J., Kneib, J.-P., et al. 2015 *ApJ*, 815, 48, doi: 10.1088/0004-637X/815/1/48

APPENDIX

A. LINE LIST

Table A1 Emission Line List

Name (* Unavailable in MaNGA; † Unavailable in SDSS)	Vacuum Wavelength	Flux Tie	Integration Range	Dispersion Tie A B ¹²	In Low EW Sample (H β EW < 10)
[C III] 1906 ^{*†}	1906.680	-	1902.2 – 1907.6	[0.57 - 1.75] (H α H β)	No
[C III] 1909 [*]	1908.734	-	1907.6 – 1914.7	[C III] 1906	No
[C II] 2325C ^{*†}	2326.113	-	2320.6 – 2326.4	[C II] 2325D	No
[C II] 2325D ^{*†}	2327.645	-	2326.4 – 2328.3	[0.57 - 1.75] (H α H β)	No
[C II] 2328 ^{*†}	2328.838	-	2328.4 – 2331.8	[C II] 2325D	No
[FE II*] 2365 ^{*†}	2365.552	-	2361.9 – 2368.6	[FE II*] 2396	No
[FE II*] 2396 ^{*†}	2396.350	-	2392.1 – 2400.1	[0.57 - 1.75] (H α H β)	No
[NE IV] 2423 ^{*†}	2422.560	-	2417.1 – 2424.2	[NE IV] 2425	No
[NE IV] 2425 ^{*†}	2425.140	-	2424.2 – 2430.2	[0.57 - 1.75] (H α H β)	No
[O II] 2470 ^{*†}	2471.027	-	2467.5 – 2474.8	[0.57 - 1.75] (H α H β)	No
[FE II*] 2613 ^{*†}	2612.654	-	2608.7 – 2617.2	[0.57 - 1.75] (H α H β)	No
[FE II*] 2626 ^{*†}	2626.451	-	2622.2 – 2629.5	[FE II*] 2613	No
[FE II*] 2632 ^{*†}	2632.110	-	2629.9 – 2635.4	[FE II*] 2613	No
He II 2734 ^{*†}	2733.700	-	2729.7 – 2737.7	[0.57 - 1.75] (H α H β)	No
[Mg V] 2784 ^{*†}	2783.700	-	2780.2 – 2787.2	[0.57 - 1.75] (H α H β)	No
[MG II] 2796 [*]	2796.350	-	2787.9 – 2797.7	[S III] 9533	Yes
[MG II] 2803 ^{*†}	2803.531	-	2797.7 – 2809.8	[MG II] 2796	Yes
[Fe IV] 2830 ^{*†}	2830.300	-	2827.8 – 2832.8	[Fe IV] 2836	No
[Fe IV] 2836 ^{*†}	2836.000	-	2832.8 – 2839.2	[0.57 - 1.75] (H α H β)	No
He I 2945 ^{*†}	2945.103	-	2943.1 – 2949.1	[0.57 - 1.75] (H α H β)	No
[O III] 3134 ^{*†}	3134.200	-	3126.0 – 3141.0	[0.57 - 1.75] (H α H β)	No
He I 3189 ^{*†}	3188.670	-	3178.7 – 3196.0	[0.57 - 1.75] (H α H β)	No
He II 3204 ^{*†}	3204.019	-	3195.1 – 3211.7	[0.57 - 1.75] (H α H β)	No
[Ne V] 3347 ^{*†}	3346.783	0.366 * NeV_3427	3336.7 – 3355.0	[Ne V] 3427	Yes
[Ne V] 3427 ^{*†}	3426.864	-	3415.7 – 3437.0	[0.57 - 1.75] (H α H β)	Yes
[Fe VII] 3586 ^{*†}	3586.000	-	3576.0 – 3596.0	[0.57 - 1.75] (H α H β)	No
[O II] 3727	3727.092	-	3716.3 – 3738.3	[0.57 - 1.75] (H α H β)	Yes
[O II] 3729	3729.875	-	-1.0 – -1.0	[O II] 3727	Yes
H12 [†]	3751.217	-	3746.2 – 3756.2	[0.57 - 1.75] (H α H β)	No
[Fe VII] 3760 ^{*†}	3760.000	-	3756.6 – 3766.6	[0.57 - 1.75] (H α H β)	No
H11 [†]	3771.701	-	3761.7 – 3781.7	[0.57 - 1.75] (H α H β)	No
H θ [†]	3798.976	-	3789.0 – 3809.0	[0.57 - 1.75] (H α H β)	No
H η [†]	3836.472	-	3826.5 – 3846.5	[0.57 - 1.75] (H α H β)	Yes
[Ne III] 3870	3869.860	-	3859.9 – 3879.9	[0.57 - 1.75] (H α H β)	Yes
He I 3890 [†]	3889.749	-	-1.0 – -1.0	H ζ	No
H ζ [†]	3890.151	-	3880.2 – 3900.2	[0.57 - 1.75] (H α H β)	No
[Ne III] 3969	3968.590	0.30 * NeIII_3870	-1.0 – -1.0	[Ne III] 3870	Yes
He	3971.195	-	3961.2 – 3981.2	[0.57 - 1.75] (H α H β)	Yes
He I 4027 ^{*†}	4027.175	-	4023.3 – 4031.1	[0.57 - 1.75] (H α H β)	No
[S II] 4070 ^{*†}	4069.750	-	4063.0 – 4076.0	[0.57 - 1.75] (H α H β)	No
H δ	4102.892	-	4092.9 – 4112.9	[0.57 - 1.75] (H α H β)	Yes
H γ	4341.684	-	4331.7 – 4351.7	[0.57 - 1.75] (H α H β)	Yes
[O III] 4364 [*]	4364.440	-	4356.4 – 4373.4	[0.57 - 1.75] (H α H β)	Yes
He I 4473 ^{*†}	4472.760	-	4464.2 – 4481.2	[0.57 - 1.75] (H α H β)	No
[Fe III] 4659 ^{*†}	4659.400	-	4652.7 – 4664.4	[0.57 - 1.75] (H α H β)	No
He II 4687	4687.015	-	4677.0 – 4697.0	[0.57 - 1.75] (H α H β)	Yes
[Ar IV] + He I 4713 ^{*†}	4713.300	-	4852.7 – 4872.7	[0.57 - 1.75] (H α H β)	No
[Fe III] 4742 ^{*†}	4741.500	-	4709.3 – 4717.3	[0.57 - 1.75] (H α H β)	No
H β	4862.683	-	4738.5 – 4744.5	[S III] 9533	Yes
[O III] 4960	4960.295	0.331 * OIII_5008	4919.0 – 4928.0	[O III] 5008	Yes
He I 4924 ^{*†}	4923.500	-	4950.3 – 4970.3	[0.57 - 1.75] (H α H β)	No
[Fe III] 4988 ^{*†}	4987.700	-	4984.0 – 4991.4	[0.57 - 1.75] (H α H β)	No
[O III] 5008	5008.240	-	4998.2 – 5018.2	[0.57 - 1.75] (H α H β)	Yes
[Fe II] 5018 ^{*†}	5016.250	-	5012.6 – 5019.9	[0.57 - 1.75] (H α H β)	No
[N I] 5199 [†]	5199.349	-	5189.3 – 5209.3	[0.57 - 1.75] (H α H β)	No
[N I] 5202 [†]	5201.705	-	-1.0 – -1.0	[N I] 5199	No
[Fe VII] 5723 ^{*†}	5723.200	-	5867.2 – 5887.2	[0.57 - 1.75] (H α H β)	No
[N II] 5757 ^{*†}	5757.000	-	5715.7 – 5730.7	[0.57 - 1.75] (H α H β)	No

Continued on next page

¹² A | B denotes where the line is tied. Case A is redshifts less than $z = 0.4963$, Case B is for redshifts greater than $z = 0.4963$, [n-m] signifies the range multiplied by (A|B), in all cases the velocity is tied to be equal to the line that the dispersion is tied to

TABLE A1 – continued from previous page

He I 5877	5877.252	-	5753.5 – 5760.5	[0.57 - 1.75]	(H α H β)	Yes
[Fe VII] 6086* [†]	6086.000	-	6076.0 – 6096.0	[0.57 - 1.75]	(H α H β)	No
[O I] 6302	6302.046	-	6296.0 – 6308.0	[0.57 - 1.75]	(H α H β)	Yes
[S III] 6314*	6313.500	-	6309.5 – 6317.5	[0.57 - 1.75]	(H α H β)	No
[O I] 6366	6365.536	0.32 * OI_6302	6355.5 – 6370.5	[O I] 6302		Yes
[Fe X] 6374* [†]	6374.000	-	6370.0 – 6380.0	[0.57 - 1.75]	(H α H β)	No
[N II] 6550	6549.860	0.326 * NII_6585	6542.9 – 6556.9	[N II] 6585		Yes
H α	6564.608	-	6557.6 – 6571.6	[0.57 - 1.75]	(H α H β)	Yes
[N II] 6585	6585.270	-	6575.3 – 6595.3	[0.57 - 1.75]	(H α H β)	Yes
He I 6680* [†]	6679.750	-	6674.7 – 6684.7	[0.57 - 1.75]	(H α H β)	No
[S II] 6718	6718.295	-	6711.3 – 6725.3	[0.57 - 1.75]	(H α H β)	Yes
[S II] 6733	6732.674	-	6725.7 – 6739.7	[0.57 - 1.75]	(H α H β)	Yes
He I 7068 [†]	7067.657	-	7057.1 – 7077.1	[0.57 - 1.75]	(H α H β)	No
[Ar III] 7138	7137.760	-	7127.8 – 7147.8	[0.57 - 1.75]	(H α H β)	No
[O II] 7321* [†]	7321.200	-	7316.6 – 7325.8	[Ar III] 7138		No
[O II] 7332* [†]	7332.200	-	7327.4 – 7337.0	[0.57 - 1.75]	(H α H β)	No
[Ar III] 7753 [†]	7753.240	-	7743.2 – 7763.2	[0.57 - 1.75]	(H α H β)	No
P η [†]	9017.384	-	9007.4 – 9027.4	[0.57 - 1.75]	(H α H β)	No
[S III] 9071 [†]	9071.100	0.41 * SIII_9533	9061.1 – 9081.1	[S III] 9533		Yes
P ζ [†]	9231.546	-	9221.5 – 9241.5	[0.57 - 1.75]	(H α H β)	No
[S III] 9533 [†]	9533.200	-	9525.5 – 9540.9	[0.57 - 1.75]	(H α H β)	Yes
P ϵ [†]	9548.588	-	9540.9 – 9556.3	[0.57 - 1.75]	(H α H β)	No

B. CATALOG TABLES

Table B1
Emission Line Catalog Descriptions

Column Name	Unit	Format	Column Description
PMF_STRING	-	STRING	The combined Plate-MJD-Fiber of the spectrum
PLATE	-	STRING	The Plate
MJD	-	STRING	The Modified Julian Date of when the spectrum was taken
FIBER	-	STRING	The Fiber
Z	-	DOUBLE	The redshift
SC_VELOCITY	km s ⁻¹	DOUBLE	The stellar continuum velocity as measured by the DAP
SC_VELOCITY_ERR	km s ⁻¹	DOUBLE	The error in the stellar continuum velocity as measured by the DAP
SC_DISPERSION	km s ⁻¹	DOUBLE	The stellar continuum dispersion as measured by the DAP
SC_DISPERSION_ERR	km s ⁻¹	DOUBLE	The error in the stellar continuum dispersion as measured by the DAP
SC_CORRECTION	km s ⁻¹	DOUBLE	The stellar continuum correction
SNR	-	DOUBLE	The median S/N ratio of spectrum
LINEID_FLUX	10 ⁻¹⁷ erg s ⁻¹ cm ⁻²	DOUBLE	The flux of a line given by LINEID as seen in Table A1
LINEID_FLUX_ERR	10 ⁻¹⁷ erg s ⁻¹ cm ⁻²	DOUBLE	The error in flux of a line given by LINEID as seen in Table A1
LINEID_EW	Å	DOUBLE	The restframe Gaussian equivalent width of a line given by LINEID as seen in Table A1
LINEID_EW_ERR	Å	DOUBLE	The error in the restframe Gaussian equivalent width of a line given by LINEID as seen in Table A1
LINEID_INT_EW	Å	DOUBLE	The restframe integrated equivalent width of a line given by LINEID as seen in Table A1
LINEID_INT_EW_ERR	Å	DOUBLE	The error in the restframe integrated equivalent width of a line given by LINEID as seen in Table A1
LINEID_SIGMA	km s ⁻¹	DOUBLE	The σ of a line given by LINEID as seen in Table A1
LINEID_SIGMA_ERR	km s ⁻¹	DOUBLE	The error in σ of a line given by LINEID as seen in Table A1
LINEID_SIGMA_CORR	km s ⁻¹	DOUBLE	The correction for the σ of a line given by LINEID as seen in Table A1

Table B2
Spectral Index Catalog Descriptions

Column Name	Format	Column Description
PMF_STRING	STRING	The combined Plate-MJD-Fiber
PLATE	STRING	The Plate
MJD	STRING	The Modified Julian Date
FIBER	STRING	The Fiber
Z	DOUBLE	The redshift
SNR	DOUBLE	The median S/N of spectrum
SPIND	DOUBLE	The value of the Spectral Index given by the Index column in Table 4 of K. B. Westfall et al. (2019)
SPIND_ERR	DOUBLE	The error in the Spectral Index given by the Index column in Table 4 of K. B. Westfall et al. (2019)
SPIND_CORR	DOUBLE	The correction for the Spectral Index given by the Index column in Table 4 of K. B. Westfall et al. (2019)

Table B3
Template Weight Catalog Descriptions

Column Name	Format	Column Description
PMF_STRING	STRING	The combined Plate-MJD-Fiber
PLATE	STRING	The Plate
MJD	STRING	The Modified Julian Date
FIBER	STRING	The Fiber
E(B-V)	DOUBLE	The E(B-V) of the Milky Way at the position of the spectrum, see Step (2) in §3.3
RCHI2	DOUBLE	The reduced χ^2 of the best fit of the spectrum found by the eBOSS-DAP
FIBERMASKED	BOOLEAN	Flag for spectra that were masked with a full fiber mask, see §3.2.1
SpecAgeX-XXXXMetY-Y.fits_wgt	DOUBLE	The weight given to the template with the age X.XXXX in Gyr and metallicity Y.Y in solar metallicity units.
SpecAgeC-XXXXMetY-Y.fits_wgt	DOUBLE	The weight given to continuous templates with the age 0.XXXX in Gyr and metallicity Y.Y in solar metallicity units.
multicoeff_N	DOUBLE	The polynomial coefficient of the Nth order with units identical to the spectrum.

C. ADDITIONAL PLOTS

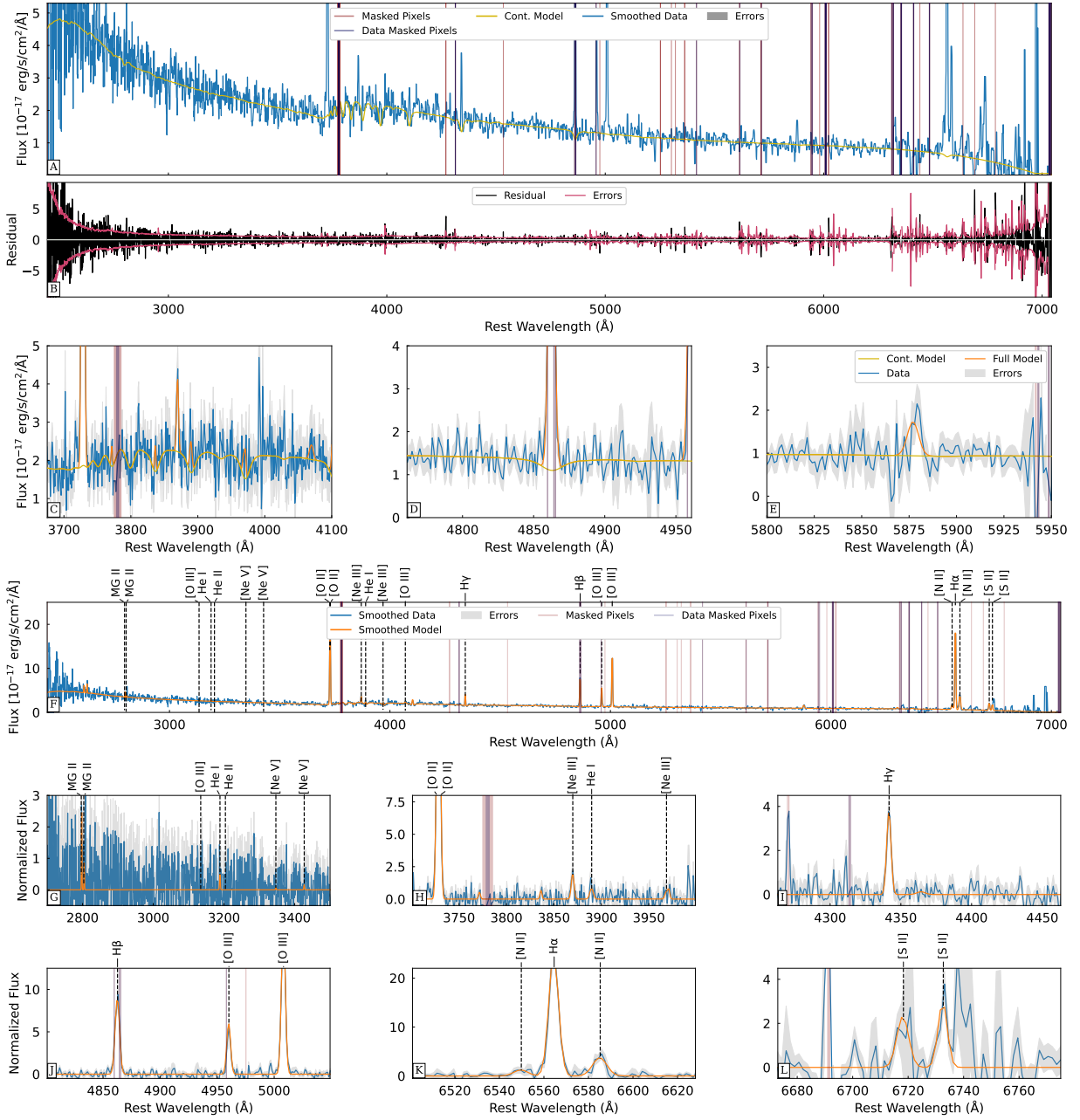


Figure C1. Sample star-forming galaxy fit for the spectra spec-7386-56769-0560.fits, which was categorized as an SFG using the BPT AGN Diagnostic. All plotting information is identical to figure 12.

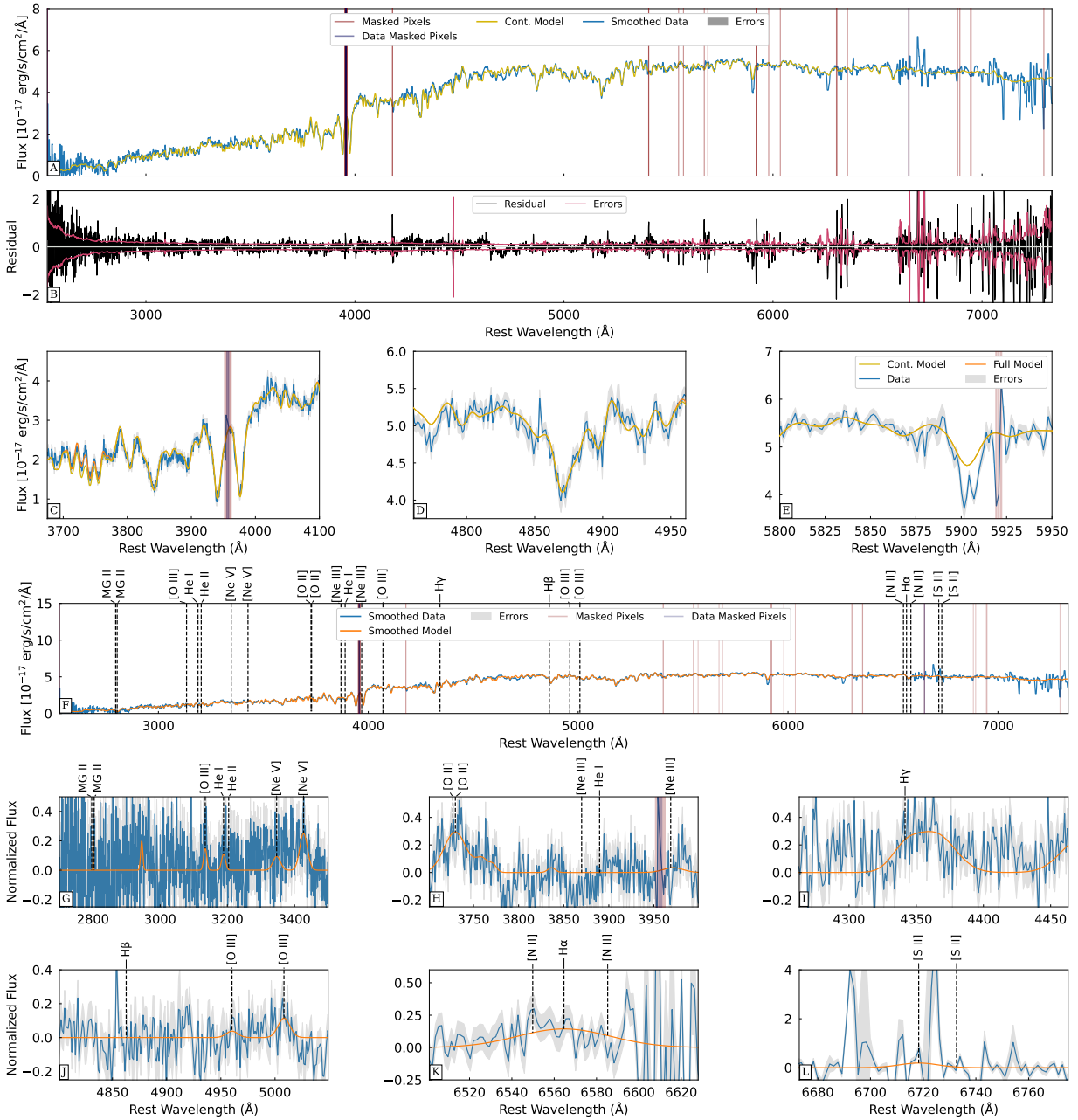


Figure C2. Sample galaxy fit plots for the spectra spec-6138-56598-0432.fits, which we classified as a red dead galaxy. All plotting information is identical to figure 12.